

An Empirical Pixel-Based Correction for Imperfect CTE. I. HST's Advanced Camera for Surveys¹

Jay Anderson *and* Luigi R. Bedin

Space Telescope Science Institute, Baltimore, MD 21218, USA; jayander,bedin@stsci.edu

Received *2010 March 23*; accepted *2010 July 21*

ABSTRACT

We use an empirical approach to characterize the effect of charge-transfer efficiency (CTE) losses in images taken with the Wide-Field Channel of the Advanced Camera for Surveys. The study is based on profiles of warm pixels in 168 dark exposures taken between September and October 2009. The dark exposures allow us to explore charge traps that affect electrons when the background is extremely low. We develop a model for the readout process that reproduces the observed trails out to 70 pixels. We then invert the model to convert the observed pixel values in an image into an estimate of the original pixel values. We find that when we apply the image-restoration process to science images with a variety of stars on a variety of background levels, it restores flux, position, and shape. This means that the observed trails contain essentially all of the flux lost to inefficient CTE. The Space Telescope Science Institute is currently evaluating this algorithm with the aim of optimizing it and eventually providing enhanced data products. The empirical procedure presented here should also work for other epochs (eg., pre-SM4), though the parameters may have to be recomputed for the time when ACS was operated at a higher temperature than the current -81° C. Finally, this empirical approach may also hold promise for other instruments, such as WFPC2, STIS, the ACS's HRC, and even WFC3/UVIS.

KEYWORDS: techniques: Data Analysis and Techniques, Astronomical

Instrumentation

¹Based on observations with the NASA/ESA *Hubble Space Telescope*, obtained at the Space Telescope Science Institute, which is operated by AURA, Inc., under NASA contract NAS 5-26555.

1. INTRODUCTION

It is well known that when energetic particles impact CCD detectors, they can displace silicon atoms and create vacancies (defects) in the silicon lattice. During the read-out process, these defects can temporarily trap electrons, causing some of a pixel’s charge to arrive late at the read-out register, and thus to be associated with a different pixel. These transfer imperfections are generally referred to as CTE (charge-transfer efficiency) losses or CTI (charge-transfer inefficiency), since some flux that was initially in one pixel gets delayed during the transfer process and shows up in a pixel that is read out later, sometimes much later. Detectors in the harsh radiation environment of space suffer this degradation much faster than detectors on the ground, making it a particularly serious problem for the aging instruments on board the Hubble Space Telescope (HST). The ubiquitous CTE-related trails stand out clearly in post-repair images taken with the Advanced Camera for Survey’s Wide Field Channel (ACS’s WFC). Figure 1 shows the upward-streaking trails in a recent short exposure.

Imperfect CTE can have two main impacts on science. First, it shifts charge from the core of a source to a trail that extends well outside of a normal photometric aperture, thus reducing the brightness measured in aperture photometry and PSF-fitting. This has a significant impact on photometry, both for point sources and for extended sources. Second, imperfect CTE blurs out the profiles of objects, shifting their centroids and increasing their FWHMs. This has a major impact on astrometric projects and on studies that involve galaxy morphology, such as weak lensing.

Because of the detrimental impact of imperfect CTE on science, much effort has been expended in order to understand what causes it and how to characterize it, both in the laboratory and by studying images taken with detectors that have suffered actual space-radiation damage. Janesick (2001, Chapter 8) summarizes the recent laboratory-based

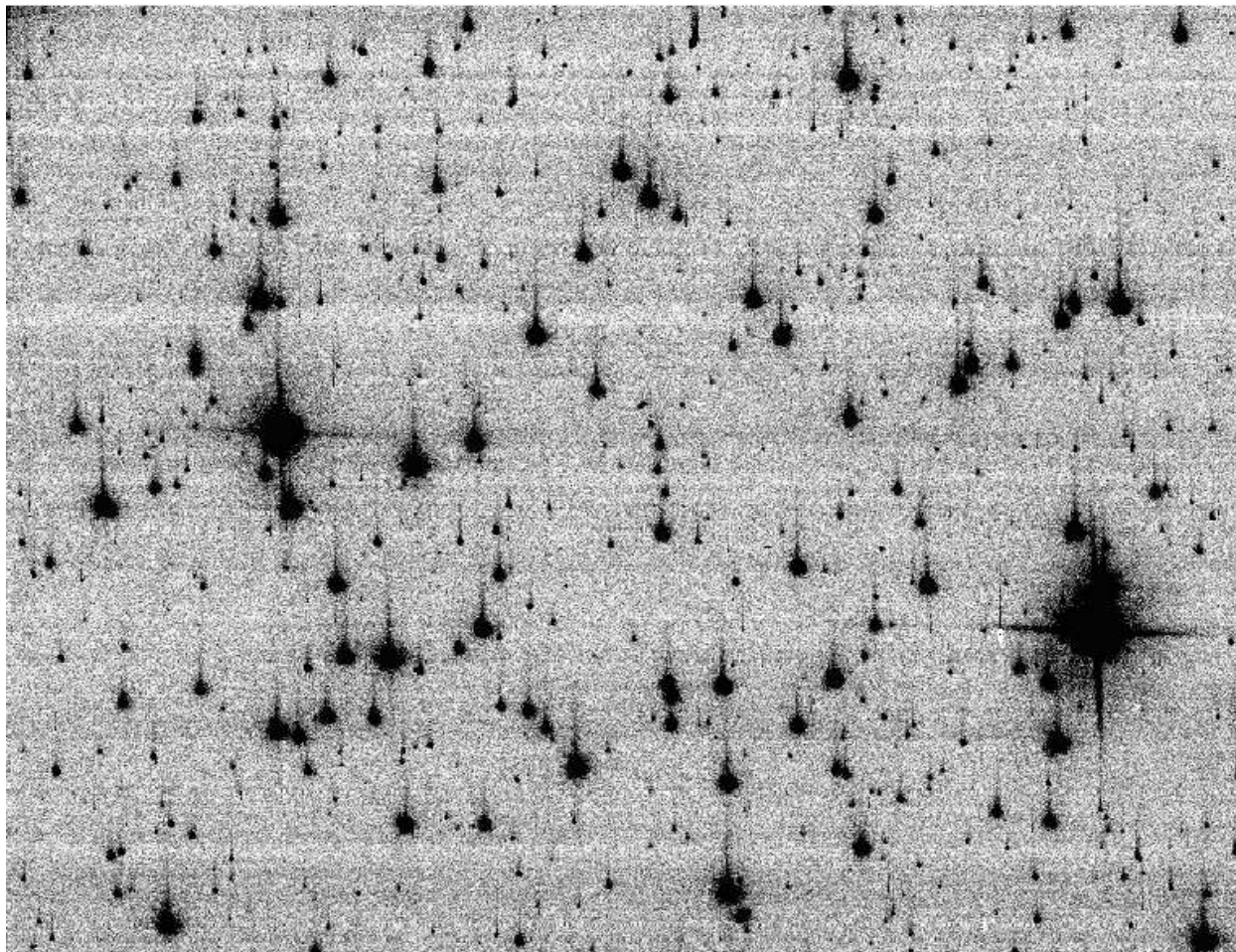


Fig. 1.— A 850×700 -pixel region centered on (1650,1725) of the bottom chip in image ja9bw2ykq_f1t, a 30 s exposure of the 47 Tuc calibration field. The background is $\sim 3 e^-$. The vertical trails extending upward from the stars are indicative of imperfect CTE; the horizontal streaks are an artifact of the post-repair readout electronics and are currently under study (Grogin et al. 2010).

research into what damage various kinds of radiation can inflict on CCDs. Although it is hard to simulate in the laboratory the exact radiation environment of space, it is possible to construct general models for how defects are generated and how they impact the transfer of charge from the pixels to the readout register. Laboratory testing has demonstrated that defects tend to capture electrons very quickly, but release them much more slowly, all with time constants that depend on temperature (see Hardy, Murowinski, & Deen 1998). The testing has also shown that charge packets with smaller numbers of electrons are exposed to a larger number of traps (per electron). These characteristics are generally consistent with our observational experience with HST, but unfortunately the laboratory tests are not yet sufficient to provide reliable quantitative predictions. This is partly because the laboratory tests cannot fully simulate realistic space environments, and partly because the laboratory tests generally rely on a limited number of photon sources (such as X-rays from ^{55}Fe) that generate fixed-size charge packets, and thus they are unable to probe the full parameter space of how charge packets of different sizes experience deferred charge. Until laboratory results are able to predict and describe the full spectrum of on-orbit CTE losses more quantitatively, we must develop empirical approaches to characterize the specific detectors currently operating in space. These approaches should be guided by the many insights gleaned in the laboratory.

Several attempts have been made over the years to empirically characterize the impact of imperfect CTE on WFC observations. A series of Instrument Science Reports (ISRs) (see Riess and Mack 2004, Chiaberge et al. 2009, and references therein) have developed empirical approaches to correcting aperture photometry. These corrections depend on the size of the aperture, the brightness of the source, the intensity of the background, and the time since exposure to the harsh environment. The losses are lower when the background is higher, which is consistent with the laboratory results that show that some of the charge traps can be filled by the background and are thus not seen by sources. These reports also

demonstrate very clearly that the amplitude of CTE losses has been increasing linearly with time, also in accord with lab results (see Fig. 8 of Waczynski et al 2001). Dolphin has made similar CTE characterizations for the WFPC2 detectors (see Dolphin 2000 and 2009).

The empirical photometric-correction trends with magnitude are sufficient for many applications, but they have their limitations. In practice the corrections are constructed only for a limited set of photometric apertures, which does not allow easy correction for stars in crowded fields or for faint stars near the background, where even a 3-pixel-radius aperture can lead to unacceptably large systematic or random errors (see Anderson et al. 2008). Furthermore, the corrections constitute average corrections and do not take into account the particular shadowing circumstances of each star (i.e., the fact that some stars may sit on higher backgrounds than others, or may have well-placed neighbors that may shield them from CTE losses). In addition, the photometric trends tell us nothing about how astrometry or an object’s shape may have been impacted by imperfect CTE. For all these reasons, over the years many attempts have been made to come up with a pixel-based CTE-correction: a way to reconstruct the original image based on the observed image and a model for CTE.

Riess (2000) studied empirical galaxy profiles in WFPC2 images and constructed a model of the readout that reproduced the phenomenology he observed in images, but the algorithm was too slow to be used in practice (Riess, personal communication). For STIS, Bristow & Alexov (2002) and Bristow (2003a, 2003b) developed a theoretical model for how charge is read out from the detector, based on lab experiments and a theoretical charge-trapping and -emission model from Philbrick (2001). They used experimental data, such as trap densities, release time constants, and the design specs for a “notch” channel (which was intended to insulate the smallest charge packets from CTE losses) to construct a computer program that simulated the STIS readout. They use this routine to generate

a realistic simulation model of lab data, then used the model to generate a pixel-by-pixel correction for science images that did a good job qualitatively removing the CTE trails. Nevertheless, despite this æsthetic success, the algorithm was not able to restore all the flux to the rightful pixels and was too computationally slow to be practical, so the standard CTE-mitigation procedure for STIS to this day still involves measuring quantities on the uncorrected pixels and applying parametrized corrections based on background, source flux, and aperture size. This is similar to what is done for ACS and WFPC2. We note that, unlike ACS, STIS can be read out using the amplifiers at any of its four corners, which makes its CTE much easier to measure and evaluate (see Goudfrooij et al. 2006).

More recently, Massey et al. (2010) have constructed a pixel-based CTE correction for ACS’s WFC for their reductions of the COSMOS fields. They use power laws and exponentials to model the amplitude and profiles of the CTE-related trails behind warm pixels (hereafter, WPs). They find that their pixel-correcting procedure is able to remove the visible trails and reconstruct the images of their targets of interest (resolved galaxies), with the result that the galaxies near the top of the chips, which are farthest from the readout amplifiers and naturally suffer more CTE losses, have shapes after correction that are similar to those at the bottom of the chips, which suffer less CTE losses. The Massey et al. correction was tailor-made for the particular characteristics of the COSMOS field: a flat background of about $50 e^-$ and relatively faint sources. They make no claims as to how well their algorithm would perform on the full range of backgrounds and source brightnesses of fields studied with the WFC. It is also not clear whether their corrections yield accurate photometry and astrometry, since they did not have access to true fluxes and positions against which they could compare their results. Nevertheless, the clear success of their algorithm at removing the trails and restoring flux to galaxy profiles is an extremely encouraging indication that a pixel-based correction for CTE is possible.

To that end, we decided to carry their study to the next level. Our aim is to characterize the impact of imperfect CTE over the full range of background intensity and source flux. Our plan will be as follows.

Although Massey et al. (2010) were able to successfully model the trails in terms of exponentials with experimentally motivated drop-offs, we will deal with the trails in a purely empirical, non-parametric way. We will constrain various aspects of our model by studying how CTE impacts WPs and cosmic rays (CRs). The WPs in dark frames serve as delta functions that allow us to calibrate the size and extent of CTE trails for pixels of various flux in images that have essentially no background². The CRs allow us to examine the effects of “shadowing” on CTE. It is well known that point sources suffer lower CTE-related losses when the background is higher, but it is unclear whether the whole-chip background or the very local background is more relevant to this trend. Laboratory experiments (see Hardy et al. 1998) suggest that this is related to the trap-capture time constants for the detector, which should be very fast and almost instantaneous relative to the parallel pixel clock-time. We will use the trails from CRs to tell us whether the trap-time truly is instantaneous.

Once the shadowing properties have been characterized, we will turn our attention to the warm pixels and construct an empirical model of the WFC pixel-readout process that reproduces the observed tails behind the delta-function warm pixels. With such a model in hand, it will be straightforward to construct an iterative forward-modeling procedure to restore the observed flux to its rightful pixel. Finally, the examination of stars will provide the ultimate test. By comparing corrected fluxes and positions for stars in short and deep exposures, we will demonstrate that this correction procedure works for all backgrounds

² Note we will refer here to all pixels with a discernible dark-current excess as “warm”, irrespective of whether the ACS Instrument Handbook would formally characterize them as “hot” ($> 0.08 e^-/\text{pix/s}$), “warm” (0.04 to $0.08 e^-/\text{pix/s}$), or below these thresholds.

and fluxes.

This paper is organized as follows. In Section 2, we first analyze a set of 168 calibration images that were taken between September and October 2009 to measure the dark current. We produce a stacked dark image and maps of where the persistent warm pixels are located. The stacks provide a high S/N profile of each charge trail, and we combine the many trails to examine trends in trail-profile shape and intensity as a function of WP intensity. In Section 3, we develop an empirical model of the readout process, putting together everything we have learned thus far, from laboratory experiments, from previous ISRs, papers, and our own qualitative analysis. The parameters of this model are optimized empirically by fitting the warm-pixel trails in the dark exposures. We test the efficacy of the algorithm for warm pixels in images with different backgrounds. In Section 4, we present the stellar tests, demonstrating that the algorithm properly returns flux to the rightful pixels so that astrometry, photometry, and even shape are restored. Section 5 discusses some improvements that could be made to make the algorithm better. Finally, Section 6 summarizes these results and considers the next logical steps to take.

2. DARK-CURRENT OBSERVATIONS

Most of HSTs orbits experience some occultation by the earth. The observatory regularly takes advantage of this “down” time to collect a rich assortment of bias frames, dark frames, and flats. As a result, the archive contains an enormous number of such calibration data sets. Over the 55 days between 4 September 2009 and 28 October 2009, there were 168 dark exposures taken. These dark exposures were between 1000 s and 1090 s in length, with an average exposure time of 1061.2 s. The darks were generally paired with bias exposures, making it easy to select a set of darks and biases for the same period of time.

2.1. The Dark-Current Dataset

We will begin our investigation using the `_raw` dark-current observations. These are 4144×4136 two-byte unsigned-integer images that contain the raw number of counts recorded by the A/D converter for each pixel. Figure 2 provides a useful schematic for these extended images. The physical pre-scan on the right and left corresponds to 24 actual pixels that are not exposed to the sky but are still read out like normal pixels. The pre-scan pixels are closest to the read-out amplifier for each quadrant. The 20 pixels of virtual overscan (in the middle of the figure, farthest from the serial registers at the top and bottom) are not real pixels, but rather come from 20 extra parallel clockings of the rows. The charge packets corresponding to these pixels start with no charge, but can gain charge on account of electrons released from CTE-traps or CRs that impact during readout. From Mutchler & Sirianni (2005, p3), we find that the serial shift time is $22 \mu\text{s}$, and the parallel shift time is $3212 \mu\text{s}$, so that the entire array is read out in $(20+2048) \times (3212 + 22 \times (2048+24)) \mu\text{s}$, or about 100 seconds.

In addition to trapping electrons during readout, defects caused by radiation damage also allow electrons to “hop” from the silicon valence band to the conduction band, thus increasing the dark current (Sirianni et al 2007). The typical post-SM4 dark current in the WFC is $0.006 \text{ e}^- \text{ s}^{-1}$ per pixel, but after many years of exposure to radiation, every pixel has a different radiation history and a different dark-pixel intensity. About 10% of the pixels have more than $0.015 \text{ e}^- \text{ s}^{-1}$, and 2% have more than $0.05 \text{ e}^- \text{ s}^{-1}$. The plentiful dark exposures contain a wealth of data about the detector defects and about the cosmic-ray intensity and frequency. The left panel of Figure 3 shows a single dark exposure (`jbanaan2q`, the first one in our list). In general, WPs are the single-pixel events and cosmic rays are the multiple-pixel events, with the typical CR affecting about 8 pixels. The field shown covers a region near the top of WFC2 (the bottom chip), and is therefore about 2000 pixels from

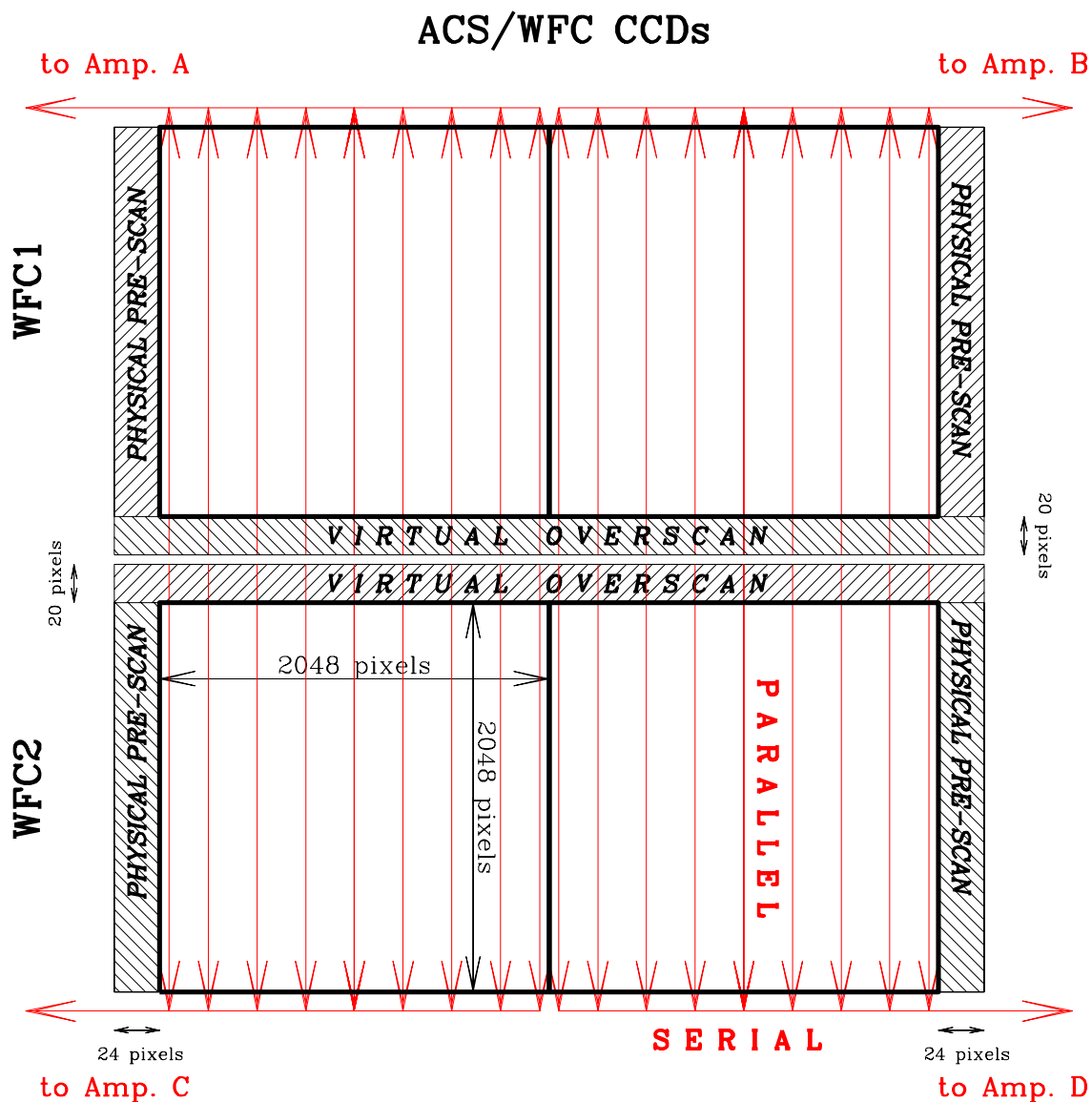


Fig. 2.— The set-up of the physical pre-scan and virtual overscan regions in the 4144×4136 `_raw` images, relative to the readout directions. The charge is first shifted along the parallel direction into the serial register, then this charge is shifted horizontally into the readout amplifiers, labeled A, B, C and D. The `_flt` images include only the 4096×4096 white region.

the bottom serial register. As such, this region suffers maximally from CTE losses and the WP trails are quite obvious.

2.2. Image analysis

We will use these 168 images in two ways. First we will distill them into two useful composite images that will help us study the average behavior of the WPs. Then later we will study them individually to understand what the transient component (namely, CRs) can tell us.

The first useful composite image we generated is a simple stack that shows the average dark frame. We construct this by normalizing the 168 `_raw` images to the average exposure time of 1060 s, then for each of the 4144×4136 pixels, we list the 168 values and compute a robust average value by iteratively clipping the values beyond $4\text{-}\sigma$. The result of this is the image shown in the middle panel of Figure 3. The CRs are gone, and the trails from the WPs are clear.

The second useful image is what we call a “peak map”. To construct this map, we go through each individual dark exposure and identify all the local maxima (any pixel greater than its 8 surrounding neighbors). The peak map records how many of the 168 images have a peak in each of the 4144×4136 pixels. This map is shown in the right panel of Figure 3 and identifies the locations of the persistent warm pixels. There are 3.3×10^5 WPs found in 150 or more out of 168 exposures, 5.3×10^5 found in more than 125, and 7.2×10^5 found in more than 100. The WPs selected in this way typically have intensities of 15 DN_2 or more³.

³ We note here that the `_raw` frames were all taken with `gain=2` so that the images could probe the entire dynamic range of $\sim 85,000 \text{ e}^-$. As such, each count corresponds to 2 electrons. To emphasize this, we refer to the count units as DN_2 , when appropriate. In

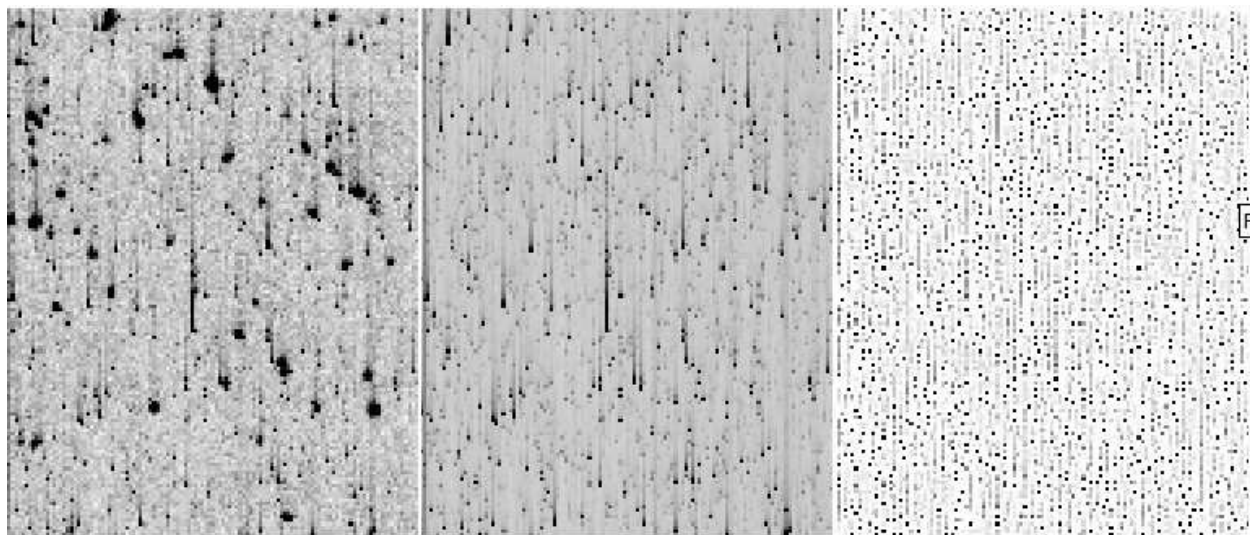


Fig. 3.— We show a 50×75 pixel region near the top of WFC2 (the bottom chip). The left panel shows a single dark exposure (`jbanaan2q`). The middle panel shows the average for all the 168 darks considered. The right panel shows the corresponding peak map. The darkest points correspond to pixels found to be local maxima in more than 150/168 exposures. The trails show up faintly in the peak map, as they are slightly more likely than other pixels in their row to be local maxima.

Because of crowding and read-noise, the WPs much fainter than this do not generate peaks in more than 100/168 exposures, making them hard to study this way.

We made an initial bias correction for each frame using the physical pre-scan pixels. Unfortunately, this does not remove all the bias, so we processed the contemporaneous bias `_raw` frames as above for the darks, and generated an average image of the bias. This average image contains a significant gradient, which increases in x and y away from the readout registers. According to Golimowski et al. (2010), these x and y gradients are due to a “bias drift” in the readout voltage, and are not indicative of actual electrons being transferred by the detector. Therefore, we simply subtracted this average bias from the dark frame before continuing with the analysis.

2.2.1. Quantitative trails

We used the peak map to identify the consistently warm pixels (those that stood out in at least 100 out of 168 exposures). In order to maximize the CTE signature, we examined the pixels that were at least 1500 pixels from the serial registers: $j > 1500$ in the WFC2 (the bottom CCD) and $j < 500$ in the WFC1 (the top CCD).

The next step is to measure the CTE trails. The schematic in Figure 4 illustrates which pixels we used to extract the CTE-release profiles upstream of each warm pixel. The profiles have been zeropointed by subtracting a “sky” value for each pixel in the trail by taking a sigma-clipped average of the ten surrounding pixels in its row (this conveniently mitigates the impact of the horizontal streaks caused by $1/f$ noise in the new signal-processing

general, the analysis in this section and the beginning of Section 3 will use the `_raw` images and will involve DNs, but beginning in Section 4, we will study the `_flt` images, where electrons are the natural unit.

electronics, see Grogin et al. 2010).

Figure 5 shows the trails quantitatively. The CTE correction we implement will be based directly on profiles like these and will be tested by its ability to remove them from images. The trails have been grouped in terms of the intensity of the warm pixel (labeled at the upper right in each panel). The pixel value for the trail is listed on the left. The percentage of WP flux in the first pixel in the trail is listed on the right. This percentage goes from 20% for low-intensity WPs to 1% for WPs that reach a good fraction of full-well. The fraction in the second pixel is down by about a half from that in the first pixel.

In addition to the fraction of flux in the trail changing dramatically with WP intensity, the shape also appears to change with WP intensity. The blue dotted line corresponds to the curve for 10,000 DN_2 , and it has been scaled to match the YU1 flux in the different profiles. While the trails do have the same general monotonic shape, the exact shape can differ by more than 10%. When we integrate this difference down the trail (note that the horizontal scale in Figure 5 is logarithmic), we find that this could account for several tens of percent in trail flux.

The red curve in the bottom right panel fits the 10,000 DN_2 profile with dual exponentials, the inner exponential constrained to fit the inner two points, and the outer exponential constrained to fit the outer half of the points. It is clear that this does a very poor job representing the trail in the middle region. Modeling the trails with simple dual-exponentials could clearly introduce errors of several tens of percent in the total trail flux.

Finally, we note that the zeropoint for the faint-WP curves dips systematically below zero beyond where the trail can be measured. This is simply an artifact of the difficulty in defining a sky value to better than 0.2 DN_2 in the images. While the images are putatively empty, the interacting trails from all the warm pixels leave a vertically coherent background

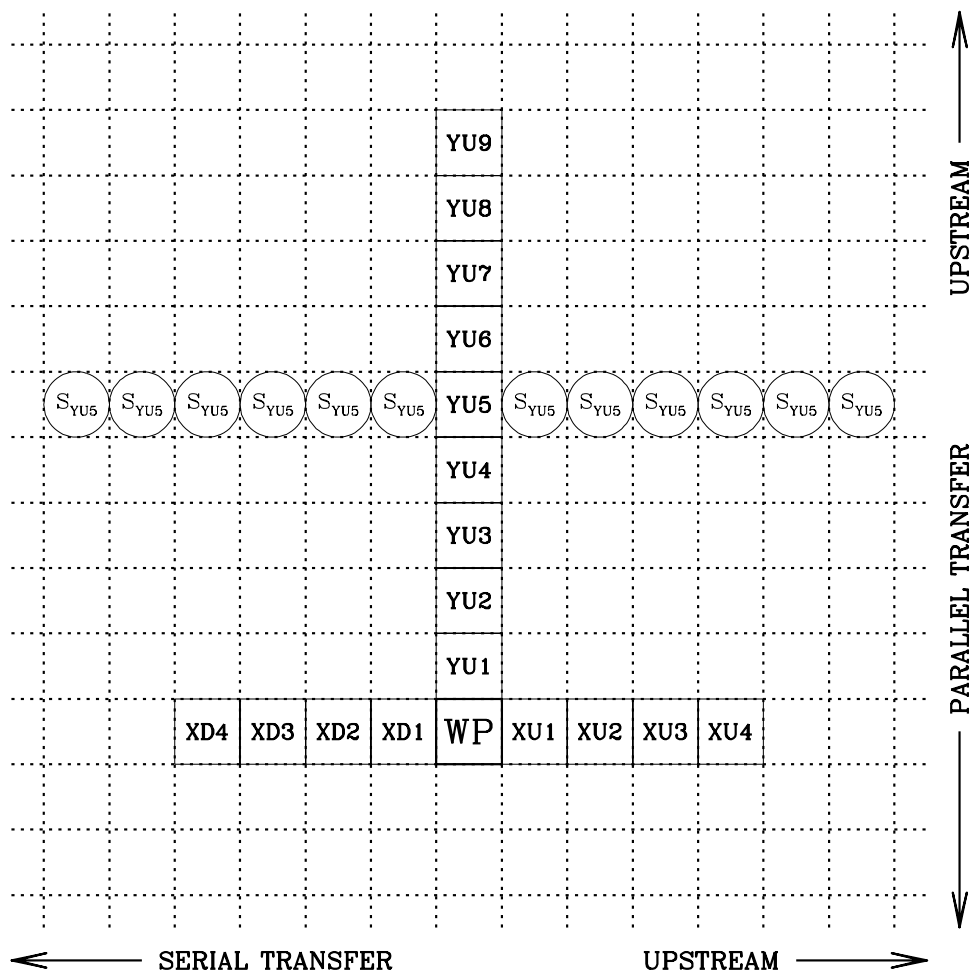


Fig. 4.— This schematic shows the pixels used to construct the CTE-release trails. The WP label indicates the location of the warm pixel. The parallel and serial transfer directions are indicated on the right and bottom, respectively. The YU_n pixels are the upstream pixels that make up the Y-CTE trail. The circled pixels are used to compute a sky-background correction for the fifth upstream pixel, $YU5$. The upstream and downstream pixels in x are also indicated.

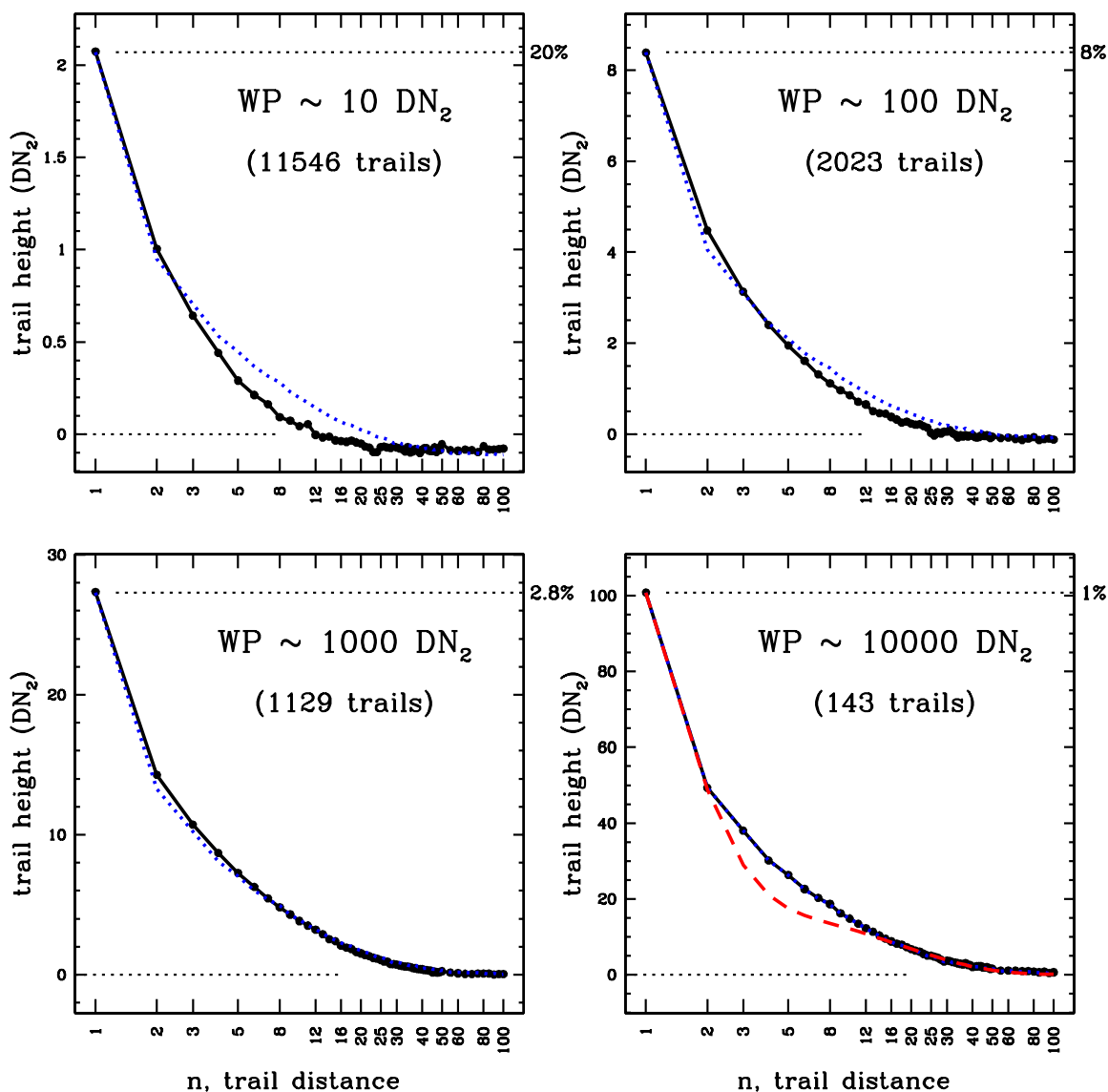


Fig. 5.— The average extracted profiles for trails behind warm pixels with intensities in the range of 10 ± 1 , 100 ± 10 , $1,000 \pm 200$, and $10,000 \pm 2500$ DN₂ that were at least 1500 pixels from the readout registers. The fraction of flux in the first upstream pixel (YU1) goes from 20% to 1%. The dotted blue curve shows the WP=10,000 profile, scaled to best match the other panels. The red dashed curve in the lower-right panel shows a dual-exponential fit constrained to match the inner and outer parts of the profile.

that does not correspond to a Gaussian distribution with a mean of zero. This makes it difficult to accurately measure flux far down the faint trails.

3. OUR EMPIRICAL MODEL

The previous pixel-based CTE analyses discussed in the Introduction have assumed a single trail shape for all pixel fluxes. Figure 5 shows that this does not appear to be the case: reality may be more complicated. Previous models have also treated the profiles as exponentials — or as a sum of two exponentials, since such a model is well motivated by theory and lab experiments (Massey et al 2010). The red curve in Figure 5 shows that a dual-exponential does not satisfactorily follow all the signal in the trails. Some recent lab experiments (see p820 Janesick 2010 or Table 6 in Sirianni et al 2007) have shown evidence for more than two trap species, some of which have relatively long release times. It is possible that the observed trails might be well represented by three exponentials (with different scalings), but for simplicity here we will model the profile empirically by tabulating what fraction of charge is retained and released as a function of the number of pixel-transfers. While this approach may involve more parameters than are strictly necessary, such a model is still considerably over-constrained by the plentiful data. Irrespective of how they are fit, the curves in Figure 5 clearly demonstrate that CTE losses follows regular and predictable trends.

3.1. Basic Constraints

Our modeling strategy will also take into account several basic facts about CTE that we gather from the extensive number of reports and papers that have been written about it: (1) CTE losses are lower when the background is higher; (2) CTE losses are proportionally

higher for fainter sources than for brighter sources; (3) CTE losses are directly proportional to the distance from the read-out register; and (4) CTE losses are directly proportional to the amount of time the detector has spent in the space environment.

While our model is purely empirical and does not depend on any quantitative results of lab experiments it does help to consider their qualitative results to motivate the model. It is clear that CTE losses are related to the presence of defects or “traps” in the silicon lattice of the CCD. These traps are generated when energetic photons, electrons, neutrons and ions impact the detector, thus naturally explaining the linear increase in CTE losses over time in the high-impact environment of space. When the electrons from a pixel in the array are shifted through a downstream pixel, a trap in the downstream pixel may capture an electron from the packet. This electron will be released some time later, after the packet of electrons with which it began its journey has already been transferred down several pixels. The trail profiles in Figure 5 give us a rough sense of how long (in terms of pixel-shift times) the typical trap holds the typical electron.

In general, the amount of charge in the trail tells us how many traps were encountered as the electron packet was shifted from the initial pixel to the readout register. Of course, the packet may have encountered many more faster-release traps that may give up the electrons before the charge is shifted. We can ignore these fast traps here: they will not affect the image, and furthermore we cannot hope to measure them by studying the image. On the other hand, traps that retain electrons longer than the chip-readout time will not produce measureable electrons in the trails, though they will still reduce the flux of the stars. The presence of these traps can only be inferred by comparing photometry against some absolute standard. Biretta & Mutchler (1997) show that the WFPC2 detector appears to have some extremely long traps, as evidenced by charge that persists into the next exposure. While no such extreme-late-release charge has been observed in the WFC, we will

certainly examine our photometry for losses not accounted for by the flux in the observed trails.

In Figure 6 we integrate up the flux in the trails for profiles similar to those shown in Figure 5 (but with more intermediate warm-pixel bins and plot the total amount of flux in the trail as a function of WP intensity. The loss goes roughly as the square-root of the WP intensity, but not exactly. We note that the Philbrick (2001) model discussed in Bristow & Alexov (2002) for STIS predicts that CTE losses should go as the square-root of the charge. This rough power law is also seen in the experiments shown in Figure 10 of Janesick et al. (1991). Hardy et al. (1998) simulate the distribution of charge set up within the pixel lattice between the electrodes and show that packets with a more charge occupy a larger volume, and as such are subject to more traps. The relation they find in their simulations is very similar to this power-law scaling, though the details of any relation will no doubt depend somewhat on the particular pixel geometry and voltage settings.

3.2. Instant or gradual shadowing?

Before we can correct images for imperfect CTE, we must construct a model for what the readout process does to the original pixel distribution. Modeling this process involves understanding in detail exactly when charge gets stuck in traps, and when it gets released. Lab experiments and theoretical models (see Cawley et al. 2001) predict that the probability of filling a trap is related to the local density of charge, with small packets taking longer to fill traps. However, given the slow parallel clocking speed, even small packets are expected to fill all the open traps that they can access almost instantly. Since our aim is to model the readout process on a pixel-by-pixel basis, it will matter considerably to our model whether traps are filled instantly, or whether it may take several traversing packets to fill them completely. In this section, we will use CRs in the individual dark images to evaluate

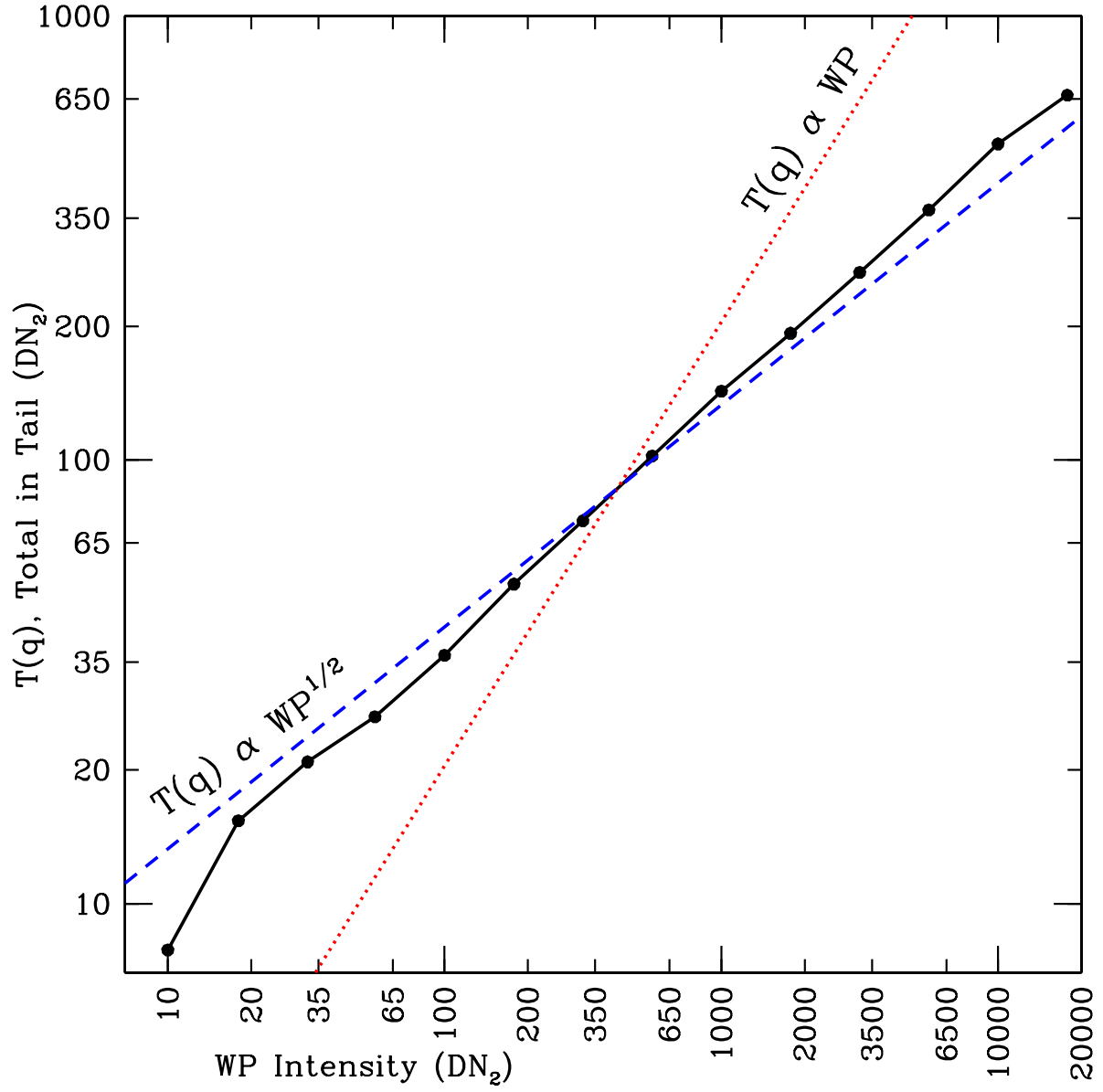


Fig. 6.— We binned the profiles shown in Figure 5 more finely and integrated up the flux in the profiles. This flux is plotted as a function of warm-pixel intensity, with a log-log scale. Lines with power-law slopes of 1.0 and 0.5 are drawn in, as labeled.

the capture-time constant empirically.

If all the accessible traps do not get filled the instant a packet passes through, then we would expect that an object with two bright pixels would experience (and fill) more traps than one with only one bright pixel. To test this, we compare the profiles upstream of WPs and CRs. The warm pixels we studied above tend to have single high pixels, surrounded by a large number of low pixels. By contrast, CRs tend to come in clumps of 8 or so impacted pixels. We analyzed each of the 168 images individually and identified bright CRs in the region at least 1500 pixels from the serial register, where CTE losses would be largest. We specifically selected CRs that had two bright pixels in the same column with nearly the same number of counts in each pixel to within 10%, with the brighter pixel being farther from the register. We further required that the CR be localized, such that the ± 5 pixels upstream of each CR had less than 5% of the total of the flux in the two bright pixels. This way, the CR should not interfere too much with the trail.

This experiment should allow us to assess whether the trail observed is more due to the sum of the pixels in an object (which would indicate a partial filling of the traps by the first pixel), or whether all the accessible traps are filled completely the moment the first charge packet passes through (in which case the trail would reflect only the bright pixel that passed over).

Figure 7 compares the trails from WPs against those for the CRs, again for events at least 1500 pixels from the readout register. The left panel shows in black the trails for WPs with intensities between 2000 and 3000 DN_2 , and the right panel shows the same for WPs between 4000 and 6000 DN_2 . The red curve shows the trails for CRs where the brightest pixel falls within the same DN_2 range. The blue curve shows the trails for CRs where the *total* of the two bright pixels falls within the same range as the WPs. We show the trails for $n \geq 3$ only because even our selections could not guarantee that there would be no flux

from the CR in neighboring pixels. (The closest few pixels to the CR maximum do tend to have the most contamination, but the contamination does not always go immediately to zero.)

It is clear that the red profiles match the warm-pixel trail almost perfectly, while the blue profiles are markedly lower. **This demonstrates that it is the flux in the brightest pixel, not the total flux, that regulates the profile of the trail.** We thus conclude that each pixel completely fills all the traps that are accessible to its electron packet, a conclusion that is consistent with the fast-fill assumption in Bristow (2002, p8). This means that while the time to release an electron from a trap can be several parallel-shift times (see Figure 5), the time it takes to fill a trap is negligibly small. This characteristic should make the charge-transfer process much easier to model, as it means that we will not have to fold into our readout model an absorption probability, which would be extremely difficult to constrain.

3.3. Statement of the model

Before we can remove the CTE effects from the observed WFC images, we must come up with a way to simulate what charge-transfer inefficiency does to observations. The model we will construct below is similar in many respects to the one constructed in Bristow et al. (2003a) and Massey et al. (2010). Many of the limitations of these models stemmed from insufficient constraints from theory and laboratory experimentation. In an effort to side-step these limitations, we adopt here a purely empirical formulation. Massey et al. developed their model using COSMOS images with a background of $51 \pm 9 e^-$ ($\sim 25\text{DN}_2$). As such, they were unable to probe CTE losses below about $100 e^-$. Since it is worthwhile to probe the trap density all the way down to zero background, we will do our analysis on the dark-exposure images. Only later will we make use of on-sky images to test the

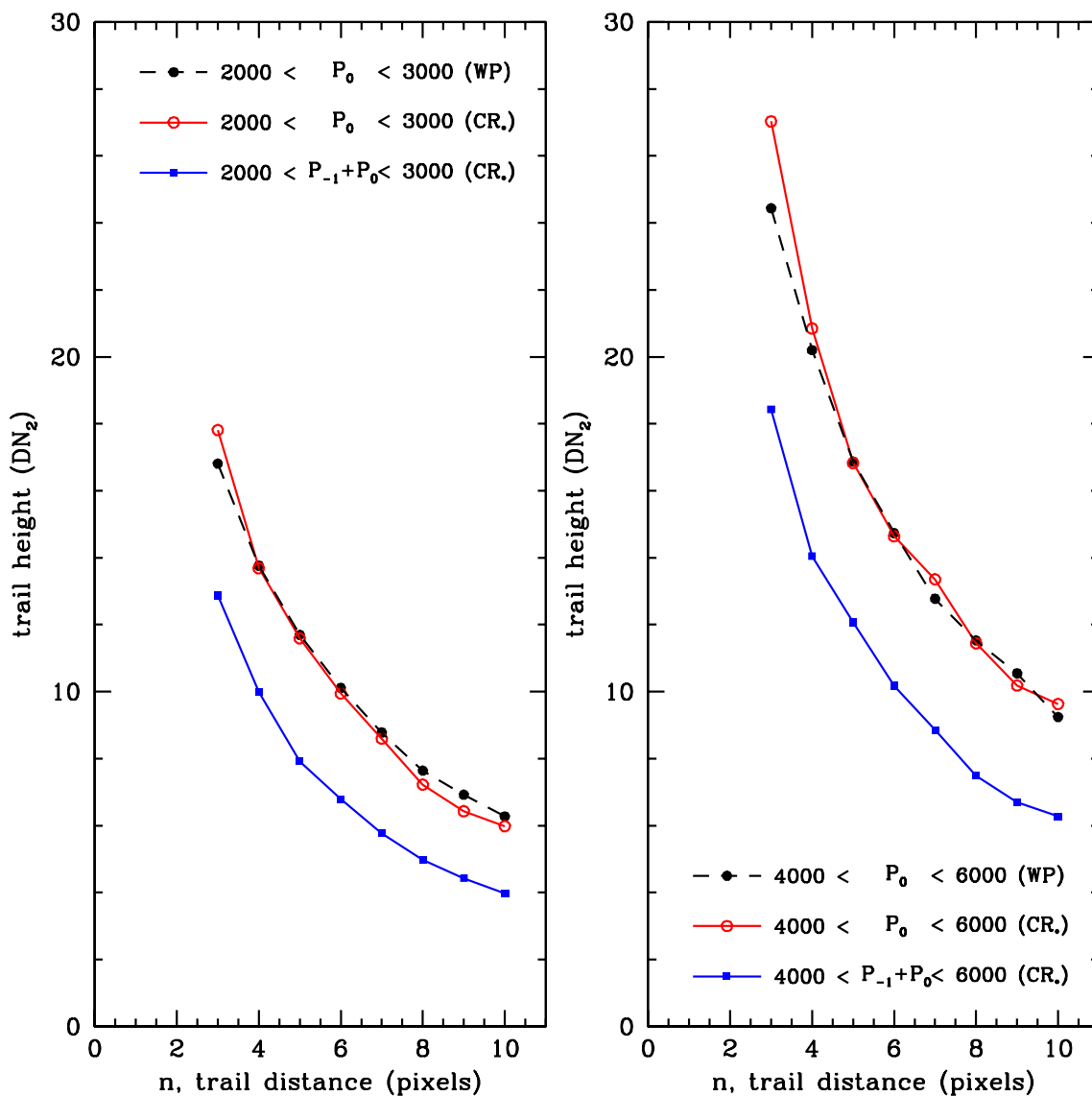


Fig. 7.— We compare the CTE-related trails for CRs chosen to have two nearly equal salient pixels against the trails for warm pixels (which have one salient pixel). CRs and WPs in the left panel have about 2500 DN₂, and those shown in the right panel have about 5000 DN₂. The trail that is observed clearly is regulated by the flux in the brightest pixel, and not the total CR flux.

algorithm. We provide a more detailed comparison between the assumptions of our model and the recent Massey model in §3.10.

Our model is quite simple. When a packet of charge is transferred through pixel B from pixel A on its way to the serial register, four things happen. The first is that the untrapped flux in Pixel B is transferred out, either to Pixel C or to the serial-readout register. The second is that the traps in pixel B that were filled previously release some of their counts. Third, the packet of charge from pixel A is transferred into pixel B, and the recently released counts in the pixel are added to it. The fourth thing that happens is that once this new packet is present in the pixel, it fills all the traps that it has access to. At this point, the untrapped charge in the packet is ready to be shifted to the next pixel. The number of counts that get transferred to the next pixel is number of counts in pixel A, *plus* the number of counts released by the traps in pixel B, *minus* the amount of charge that was newly retained by the traps in pixel B: $N_B = N_A + N_{\text{released}} - N_{\text{trapped}}$. The N_{trapped} counts will remain in pixel B until released later into a different packet, associated with a different read-out pixel.

From our experiment in §3.2, we determined that every electron that can occupy a trap, will occupy the trap instantly. This means that when a packet is in a pixel, it fills all the traps it has access to. The number of traps available to a packet is clearly a function of how many electrons are in it. Figure 6 showed that the number of traps accessible to a packet increases roughly as the square root of the number of electrons in the packet. Although this $T(q)$ curve goes nearly as the 0.5-power, it is not exact, so we will represent this relationship empirically by tabulating its value at a set of node points (10, 30, 100, 300, 1000, 3000, 10000, and 30000), using interpolation in between. We note here that the charge q here is in units of DN_2 .

In practice, we will use the differential form of this curve, the number of traps per

marginal electron, $\phi(q) = \frac{dT}{dq}(q)$. The quantity $T(q)$ plotted in Figure 6 corresponds to the total number of traps seen after about 1750 pixel shifts (we examined pixels between $j=1500$ and $j=2000$).

Calculating the number of counts released is more complicated, since charge is captured instantly, but it is released gradually. It appears from Figure 5 that the traps that affect smaller charge packets have somewhat steeper release profiles than the traps that affect only larger charge packets. This means that we may need to use a two-dimensional function to describe the release of charge. The function $\psi(n, q)$ represents the probability that a trap that affects the q^{th} charge will release its charge after the n^{th} pixel shift. The distributions from Figure 5 should give us a rough idea of the shape of $\psi(n, q)$ for various values of q .

The one aspect remaining is to remember that electrons are conserved. When an electron encounters a trap of a certain depth, there is a probability, based on the distribution of electron packets that have come before, that this trap will already be occupied. If we later transfer charge into this pixel that would like to fill the trap, we must remember that we can fill it only if it is empty. We can use the release-probability function $\psi(n, q)$ to tell us the probability that the trap will be empty, and can then fill it with a partial electron, reflecting the expectation probability of an empty trap. Hardy et al. (1998) suggest a similar algorithm.

This begs an interesting question: will the trap then release the electron according to when it was initially filled, or according to when it was last filled (or “topped off”)? We will assume here that when we fill a partially empty trap, we “reset” its release-time constant, so the only thing that matters is when it was last topped off. This is the simplest possible assumption, and it appears to be consistent with the data.

Even though all of the trap-filling and trap-releasing is surely a quantum process involving one electron at a time, for simplicity here we treat it as a continuum process,

dealing with fractional traps and fractional charge. It is also true that each pixel has a different radiation-damage history and a different distribution of traps. However, since there is currently no way for us to determine which pixels may hold traps of which depth (the density of traps is too high for pocket-pumping to yield a definitive distribution), it is reasonable to treat all pixels as having the same distribution of fractional traps.

3.4. The Detailed Readout Algorithm

The readout simulator requires two functions that describe the nature of the traps: ϕ_q and ψ_{nq} . The ϕ_q array contains the number of traps from pixel $j=2048$ to $j=1$ that catch charge between $q - \frac{1}{2}$ and $q + \frac{1}{2}$. For example, if a pixel at the top of the chip ($j = 2048$) has 100 DN_2 , then it will be subject to $\sum_{q=1}^{100} \phi_q$ traps. Integrating up our final ϕ_q array gives a value of 36.3 DN_2 of traps (see $T(q)$ in Figure 6). This means that if the background is zero and a pixel near the top of the detector starts out with 100 DN_2 , it will likely have 64 of them when it clocks out at the bottom. The trail will contain 36 DN_2 . This model only treats the charge that either stays with the pixel or ends up in the observable trail. We will see in Section 4 whether there are losses that do not show up in the observed trails.

The second function is ψ_{nq} . It gives the probability that the q^{th} charge in a packet will be released n pixels downstream. The model we adopt is able to track charge trails out to 100 pixels ($n = 100$). As we mentioned above, our model is not able to account for charge in the trails beyond this. It is possible that there are even fainter trails that extend much further, but if they are present, we will have to use a different formalism to represent them.

For each column that is read out, there are $2048 \times (2048/2) \sim 2 \times 10^6$ total pixel shifts involved. (The division by two comes from the fact that a pixel in the top row gets shifted 2048 times, and one in the bottom row only once; the typical row is therefore shifted 1024

times.) It would be computationally prohibitive to simulate each of these shifts individually for each of the 4096 columns for each chip, so we recognized that many of the shifts are identical. If we consider pixels A and B in rows $j = 1001$ and $j = 1000$, respectively, pretty much the same charge transfer takes place 1000 times: electron packet B is shifted out of a pixel, and packet A is shifted in, and if CTE is close to unity, A and B will not change very much from the top to the bottom. For simplicity, we model this as incurring $1000\times$ the CTE loss as a single-pixel transfer. This simplification increases the algorithm’s speed by a factor of ~ 1000 , and allows us to treat all pixels as having the same distribution of traps from $q = 0$ to saturation. Previous efforts (Massey et al. 2010 and Bristow et al. 2002) have assumed a specific realization of the distribution of traps throughout the chip in an effort to make the calculation computationally tractable.

Our assumption above breaks down when CTE losses begin to have a significant impact on the charge distribution, such that we might expect different transfer effects at the top of the column, where the intrinsic structure is coherent, and at the bottom of the column, where the true structure may be broadened by imperfect CTE. We recognize this potential limitation of our model, but such a situation should occur only in the more pathological situation where CTE cannot be considered a small perturbation. For computational speed in developing and converging upon our model, we will treat all pixel shifts the same, but will be careful to identify situations where this simplified treatment may be inadequate (see Section 6.2).

We simulate the column readout going from pixel $j = 1$ to pixel $j = 2048$ (or 2068 if we are including the virtual overscan). In order to monitor how long it has been since traps that affect different charge levels have been released, we maintain an internal array, n_q , which keeps track of how long it has been since the trap at each marginal charge level q was filled. At the beginning of the readout, the n_q array is set to 100 for all q , from 1 to 50,000.

This corresponds to all the traps starting out completely empty. As far as the model is concerned, it means they were last filled more than 100 transfers ago.

We now have all the elements necessary to illustrate the algorithm. We start by shifting the first pixel into the serial register. At the beginning of the readout, this pixel has P_1 DN₂ in it. We use the following equation to determine how many electrons the traps in this pixel will hold back:

$$N_{\text{trapped}} = \sum_{q=1}^{P_1} \phi_q \times \left(1 - \sum_{n=n_q}^{100} \psi_{nq} \right) \times \left(\frac{j}{2048} \right). \quad (1)$$

The first term within the main summation provides the number of traps present per 2048 pixels at each marginal charge level q . The second term (in parentheses) reports what fraction of the traps at this charge level are still unfilled. The final term scales N_{trapped} for the number of pixel shifts to the register (just j). The summation itself is over all the charge in the pixel, P_1 .

Finally, we shift $P_1' = (P_1 - N_{\text{trapped}})$ charges into the serial register, and this is what is read out by the amplifier (modulo losses from CTE in the serial direction, which we will discuss briefly in §5.3). We then reset the n_q array to 0 for all $q \leq P_1$, since the traps were just filled all the traps up to this charge level.

The next step is to determine how much charge is released by traps in the pixel before the next charge packet arrives. We do this by simply summing over the released charge, trap by trap:

$$N_{\text{released}} = \sum_{q=1}^{50,000} \phi_q \times \psi_{n_q q} \times \left(\frac{j}{2048} \right). \quad (2)$$

The summation is over all charges, from the ground to saturation. The first term scales the release for the number of traps that affect electrons at this charge level. The second term corresponds to the fraction of the charge in the trap that gets released in the n_q^{th} transfer since the trap was filled. The final scaling corresponds to the number of transfers that take

place, with a pixel at the top of the column getting a factor of 1.00.

Once the appropriate amount of charge has been released from each trap, we increment the counter for the trap at each charge level by setting n_q to $n_q + 1$. We cap n_q at 100, since our model is unable to follow the trails beyond 100 pixels, and assumes that after 100 shifts, the traps are empty.

Finally, we shift the packet of electrons from pixel $j = 2$ into this first pixel and end up with $(P'_2 + N_{\text{released}})$ charge in the pixel. At this point, the algorithm returns to the starting point above, and we determine how many electrons get captured in traps and transfer the remainder into the serial register. This process continues for the pixels from $j = 1$ to 2048 (or 2068 in the `raw` frames).

All of the dark exposures we have used here were taken at about the same time (within a two-month period in late 2009), so each exposure should suffer about the same CTE losses. It is well established (see Riess & Mack 2004 and Chiaberge et al. 2009) that CTE losses have been increasing linearly over time since ACS was installed in space during Servicing Mission 3B in 2002. For times before or after October 2009, we will need an additional multiplicative term to account for the overall scaling of trap density. This term can go after the $(\frac{j}{2048})$ terms in the N_{trapped} and N_{released} equations above:

$$\left(\frac{JD_{\text{OBS}} - JD_{\text{SM-3B}}}{JD_{10-1-2009} - JD_{\text{SM-3B}}} \right). \quad (3)$$

Since this model was developed for the October 2009 epoch, the correction factor is naturally 1.00 for the present epoch.

The adoption of the simple scaling law above implicitly assumes that nothing has changed in the detector’s CTE properties from installation to after SM4. It remains to be seen whether anneals or changes of CCD temperature have any affect on CTE trail profiles or scaling. Laboratory experimentation and theory suggest that raising the temperature

should lower the release time and thus steepen the trails. There is no reason to think that the number of traps will change within the -77°C to -81°C operating-temperature range. All these issues should be thoroughly investigated before any general, long-term implementation of the algorithm.

3.5. An Example

Figure 8 provides an example of the readout-simulating algorithm at work. On the left, we show the original pixel value (P_{ORIG}) for pixels between column index $j=2001$ and $j=2012$. We simulate here a star that has its y -center at 2007.5, with a background of 2 DN_2 .

The next column in the table, N_{REL} shows the amount of charge released due to previous charge-filling from downstream pixels, from Equation [2] above. This charge is added to that in the previous column to get the third column, P_{TEMP} . This charge fills all the holes available, which we compute from Equation [1] above. The trapped amount of charge is reported in the fourth column, N_{TRAP} . Finally, this is subtracted from the third column, to get P_{OBS} , the charge that ultimately makes it to the serial register. The sixth column Δ reports the difference between the input and output charge, $P_{\text{ORIG}} - P_{\text{OBS}}$.

The raster on the right reports the state of the charge traps. The horizontal dimension corresponds to the marginal charge (q) that the trap impacts. The number in this array (n_q) for each pixel at each charge level tells us how many transfers it has been since each trap was filled. An asterisk here means that the trap was filled more than 100 pixels ago, and it is thus empty. A 1 indicates it was filled by the previous pixel, a 2 by the pixel before that, etc. The traps within the boxed region correspond to traps that will be filled by the current pixel (regulated by P_{TEMP}), so that for the next upstream pixel, these traps

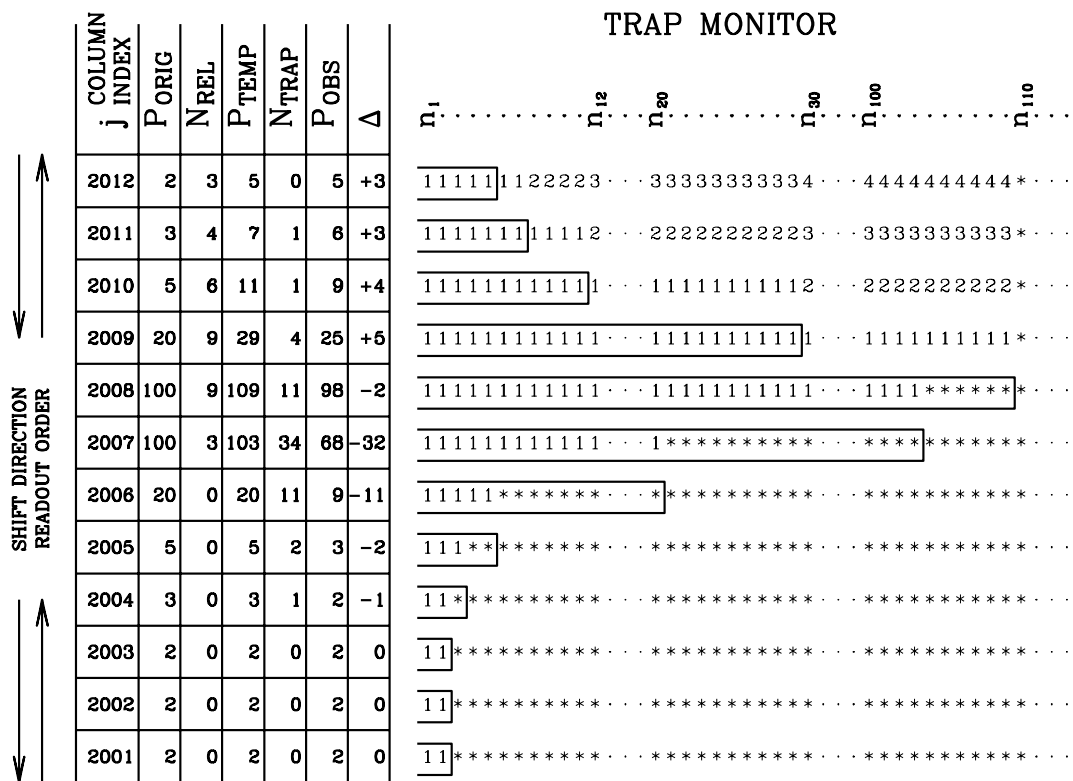


Fig. 8.— This schematic shows the inner-workings of our pixel-transfer algorithm. See the text in §3.5 for details. The asterisks in the trap monitor correspond to traps that are completely empty ($n_q \geq 100$). Numbers in the table are rounded to the nearest integer.

will begin releasing with $n_q=1$.

It is clear in this simulation that the centroid of the star moves considerably up the chip. Rather than observing the true vertical profile of $\{20, 100, 100, 20\}$, we end up observing a profile of $\{9, 68, 98, 25\}$. Note also that the first bright pixel ends up taking a large hit from imperfect CTE, losing 32 out of 100 counts, but the second one loses only 2 out of 100 counts. This is a result of the shadowing prescription implicit in our model (see §3.2).

3.6. Iterating to Find the Original Pixel Distribution

The above process tells us only what happens to an original distribution of charge in a column, P_j , as it is transferred down the column and read out as P_j' . It does not tell us how to reconstruct the original “source” pixel array, P_j , from the observed array. To do this, we must somehow invert the process. We do this in a manner similar to that in Bristow & Alexov (2002) and Massey et al. (2010) (see their Section 3.2).

We first adopt the actual observed pixel array P_{OBS} as an estimate of the original array, \hat{P}_{ORIG} . We run this through the readout simulation and arrive at a simulated observed array, P_{OUT} . This array will be less sharp than the actual observed array, since the readout process introduces CTE trails. Our goal is to find the source array that, when run through the readout process, will yield the observed array P_{OBS} . So, we adjust the source array in such a way as to bring the output array to be closer to the observed array: we add to the current source array the difference between the observed array and the output array. The following pseudo-code shows how the convergence proceeds:

```

 $\hat{\mathbf{P}}_{\text{ORIG}}^{[0]} = \mathbf{P}_{\text{OBS}}$ 
do n = 1, 5
   $\mathbf{P}_{\text{OUT}}^{[n]} = \text{COL\_READOUT}[\hat{\mathbf{P}}_{\text{ORIG}}^{[n-1]}]$ 
   $\hat{\mathbf{P}}_{\text{ORIG}}^{[n]} = \hat{\mathbf{P}}_{\text{ORIG}}^{[n-1]} + (\mathbf{P}_{\text{OBS}} - \mathbf{P}_{\text{OUT}}^{[n]})$ 
enddo.

```

The routine `COL_READOUT` takes in an array representing the original pixel values and simulates the charge-transfer process, returning the array that would be observed. In the end, $\hat{\mathbf{P}}_{\text{ORIG}}^{[5]}$ is our 5th-iteration estimate of the original pixel distribution. Most charge, even when the background is low, comes through the read-out process without being shifted, so imperfect CTE can be thought of as a slight perturbation. As such, this process converges quite quickly. We generally do 5 iterations.

One slight concern about this iterative scheme is that the flux recorded in each image pixel \mathbf{P}_{OBS} does not correspond exactly to the amount of charge in DN_2 that arrived at the register. The observed pixel value also contains a contribution from readnoise ($\sim 4.5 e^-$ for ACS’s WFC). If we operate the algorithm on \mathbf{P}_{OBS} , then the process will end up amplifying the readnoise, which may not be desired. In §5.1 we explore one way to minimize the influence of readnoise-level fluctuations on our algorithm. However, it should be safe to defer the readnoise-related issues until later, as our dark exposures have been combined into a stack that should have the noise reduced by $\sqrt{168}$.

3.7. Finding the optimal model parameters

To keep our model as simple as possible, we wanted to use the minimum number of parameters. The full model as stated would have about 5 million degrees of freedom if we

consider all the possible values of ϕ_q and $\psi_{n,q}$ for all q and n . Clearly these functions will vary smoothly with their parameters and we can represent them interpolating an adequately spaced table. To this end, we tabulate the value for ϕ_q at an array of logarithmically spaced points in q : 1, 3, 10, 30, 100, 300, 1000, 3000, 10000, 30000, and 100000 DN₂, and use log-linear interpolation to compute ϕ_q for any integer q . Similarly, we tabulate the two dimensional function ψ_{nq} at values for n shifts of 1, 2, 3, 5, 8, 12, 16, 20, 25, 30, 40, 50, 60, 70, 80, 90, and 100 pixels, and values of q of 10, 100, 1000, and 10000 DN₂. To get ψ_{nq} for any value of n and q , we interpolate linearly in the n dimension and logarithmically in the q dimension. This interpolation is done once-for-all, so that the program ends up working with arrays `phi[1:100000]` and `psi[1:100,1:100000]`. The condensed set of parameters can be conceptualized as having 79 nodes: $\Phi[1:11]$ and $\Psi[1:17,1:4]$ (the capital letters denote the node parametrization).

Unfortunately, we cannot simply take the extracted values for these functions from Figures 5 and 6 to arrive at the final model. The trail for a bright pixel generates many lower-intensity pixels in its lee. The charge released in the trail pixels is subject to the same imperfect transfer as the original charge, so there is some interplay between the bright and faint trails.

We resolved this complication by iteration. We started with the arrays as extracted directly from Figures 5 and 6. We then ran the reconstruction routine on the dark stack to see how well the trails were removed. We again constructed a plot similar to Figure 5, only this time with the reconstructed image as the source image. The remaining trends showed us how to adjust Φ_Q and Ψ_{NQ} to in such a way as to improve the fit.

It took several hands-on iterations for the model parameters to converge. We began the convergence with traps at all q levels having the same trail profile (i.e., ψ_{nq} being a function of n only). This worked well for all the traps above $q \sim 100$ DN₂, and it implies that the

slightly different profiles seen in Figure 5 may be a result of a some self-shielding within the trails. It also means that most traps, irrespective their location within the pixels, appear to have largely the same release-time profiles.

We were unable to fit the very lowest bin ($q \sim 10 \text{ DN}_2$) with the same profile, so we gave this lowest bin a steeper profile. Even with a steeper profile, we had to use an extremely high trap density (0.8) to account for the amount of charge in these trails. This means that 80% of the electrons at this charge level are likely to encounter a trap when transported from the top of the chip to the bottom. This implies a significant level of CTE losses, and a more sophisticated, non-perturbative approach may be necessary to deal properly with CTE issues at this low flux level (see the discussions in §3.4 and §6.2).

Once CTE losses reach a truly pathological level, it will no longer be possible to make any inference about the original charge distribution. This will happen when there are more traps than charge, such that most charge will be removed from its original pixel packet and can no longer be associated with its original pixel location. The deep dark images currently available may not be the best way to explore these issues, since in the 1000 s exposures, there are so many $\sim 10 \text{ DN}_2$ WPs, that it is hard to study them in isolation. Taking shorter darks should remedy this, but for the moment, we will simply adjust our model to deal with the low- q WPs as well as possible, and will see how well the algorithm can work. Improvements can be made later (see §6).

The converged-upon model parameters are shown in Figure 9. The trap density ϕ -vs- q is shown on the left. The trend largely follows $\phi_q \sim q^{-0.5}$, consistent ϕ_q being the derivative of T_q (see Figure 6). The release profiles are shown on the right, normalized to have a total probability of 1.00. The steeper profile applies for $q \sim 10$, the other for $q \geq 100$.

The first real test, of course, is how well the trails are modeled. Figure 10 shows the residuals of the trails, in the same format as Figure 5, though with twice as many

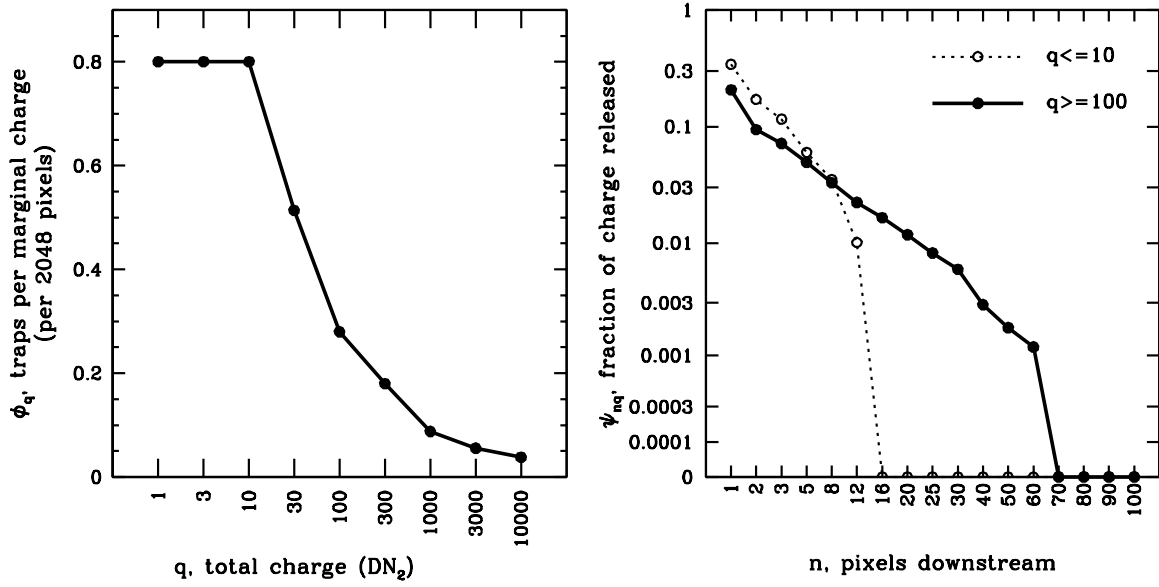


Fig. 9.— This shows the run of parameters used in the converged-upon model. On the left, we show ϕ_q , the number of traps in a column per marginal charge at q . On the right, we show the release profile for $q \leq 10$ (dotted curve) and for $q \geq 100$ (solid curve). The symbols indicate the location of the nodes used to specify the functions.

warm-pixel bins. It is clear that the trails for all levels of charge are removed cleanly. The trails appear to be removed well even in the faintest WP bin, where our algorithm has to treat larger CTE losses than it is designed for.

Figure 11 shows the before and after images centered on the same region as in Fig. 3. It is clear that we are removing a large fraction of the trails and restoring the flux to its rightful pixel — usually a single pixel in these dark, warm-pixel pocked images. Note that there is nothing in the reconstruction algorithm that would force flux back into one pixel, as opposed to two or three. The restored image is simply the one that is best able to predict the observed image. The fact in most cases that the flux was restored to a single pixel is an encouraging sign.

There are clearly some trails in the image that are over-subtracted, and others that are under-subtracted. It is interesting to note that the over-subtracted trails often lie in the same rows, as do the under-subtracted trails. A significant WP of 1000 DN_2 loses about 150 DN_2 to the trail (see Figure 6). If each trap impacts a single electron, this implies 300 traps ($1 \text{ DN}_2 = 2 e^{-1}$). If these traps are distributed randomly, we should expect a column-by-column variation in CTE losses of $\sim 5\%$. This variation would be even larger if the traps are generated in clumps, many-at-a-time. Waczynski et al. (2001) note that energetic photons and electrons tend to generate single traps, but neutrons and ions often generate multiple traps in the same pixel, such that the particular radiation environment could make CTE more variable from column to column than single-trap Poisson statistics would suggest. We can better study the statistics of trail subtraction in the individual exposures, using CRs or stars, as these (unlike the WPs) impact different places on the detector in different exposures

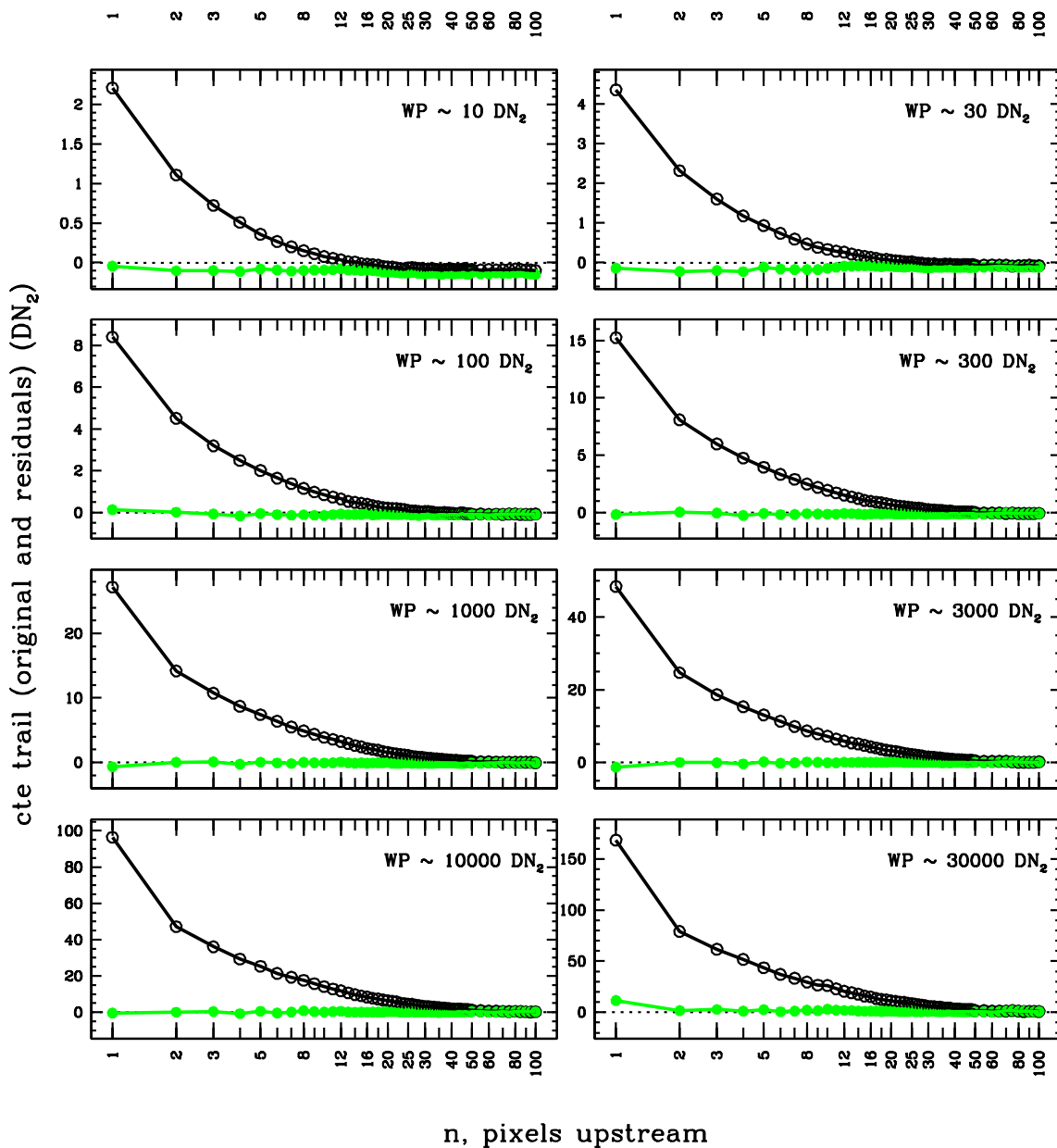


Fig. 10.— Similar to Figure 5. The original trails (black) and the residuals (green) after model-fitting for the warm-pixel stack, binned for 8 different warm-pixel intensity levels.

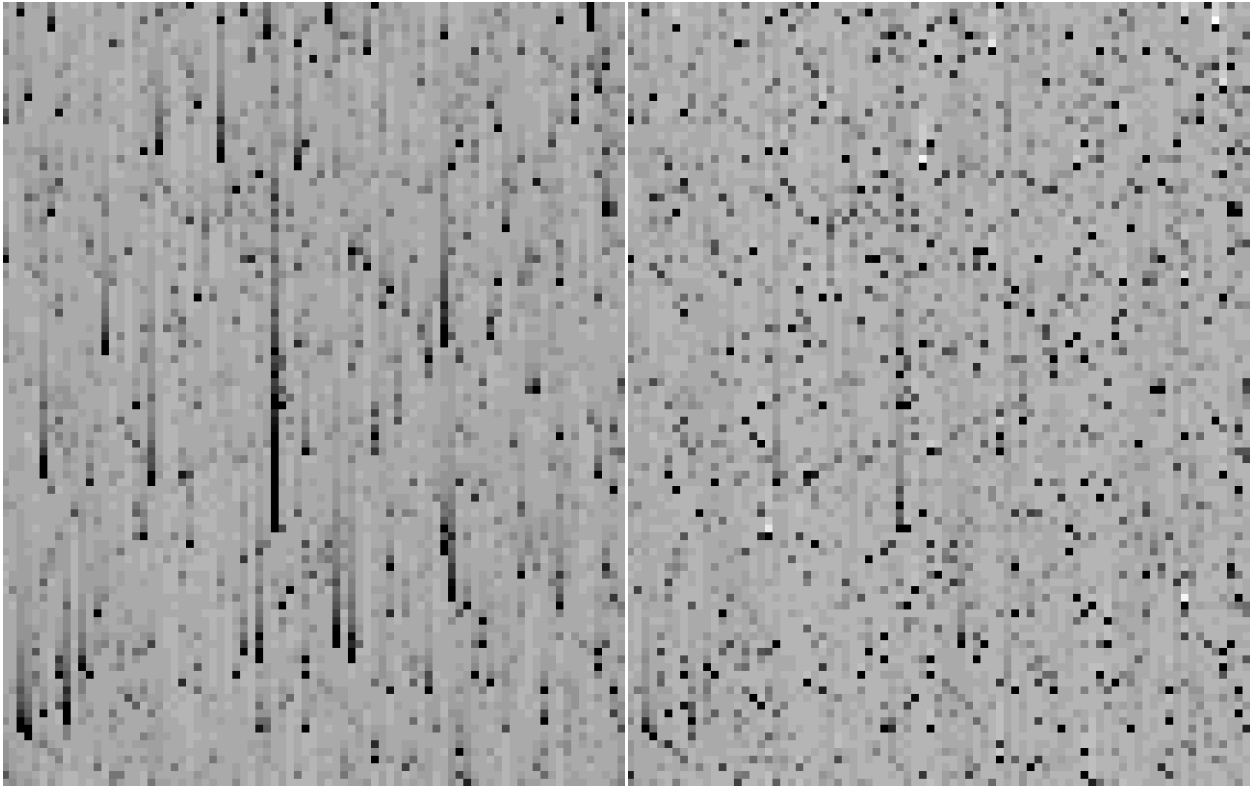


Fig. 11.— (Left) The stack of the dark exposures, after the bias has been removed. (Right) The same stack, after the pixel-based Y-CTE correction.

3.8. Limitations of the super-dark analysis

Since the dark frames have very low background and therefore suffer the largest CTE losses, it is extremely encouraging that our algorithm does so well here. Nevertheless, it will still be important to show that the parameters can work in “easier” (and more scientifically relevant) environments, as well. Thus, we will have to test the algorithm on sky-exposed images that have a variety of background intensities.

As far as what to expect with the higher background situation, we note that the model as formulated does naturally predict lower CTE losses when the background is higher, since empirically we see more traps that affect small charge packets than those that affect only large packets. When the background is high, these small-packet traps are all filled and it is only the marginal larger-packet traps that come into play.

One additional inadequacy of developing the correction on the stacked dark frame is that there are not many high-signal warm pixels. This makes it difficult to calibrate the upper end of the ϕ_q curve. In the next section, we will examine the bright end more carefully using stars in short exposures.

3.9. Final Model

The parameters of the converged-upon final model shown in Figure 9 are listed in Tables 1 and 2. These parameters, fed into the algorithm discussed in §3.4 result in a near-perfect removal of the CTE-related trails from the dark exposures. It remains to be seen whether this restorative fix is sufficient to account for *all* CTE losses. It is possible that the CTE trails could have a longer and fainter component than we can observe empirically. The final test will therefore be to run this pixel-based correction on images for which we know what the true scene should look like. This will be the focus of the next sections.

Table 1: The number of traps per marginal DN_2 , ϕ_q , from the optimized model. Recall that $1 \text{ DN}_2 = 2$ electrons.

node number	marginal DN_2	traps per DN_2
Q	q	ϕ_q
1	1	0.8000
2	3	0.8000
3	10	0.8000
4	30	0.5000
5	100	0.2800
6	300	0.1750
7	1,000	0.0880
8	3,000	0.0540
9	10,000	0.0380
10	30,000	0.0115
11	100,000	0.0060

Table 2: The measured release profile for traps at different q levels (q is in DN_2). Note the model allows release times up to 100, but we found no perceptible change in the trails beyond $n = 70$ shifts.

node	shifts	fractional release	
N	n	$\psi_{n,q \leq 10}$	$\psi_{n,q \geq 100}$
1	1	0.3417	0.2061
2	2	0.1709	0.0942
3	3	0.1156	0.0718
4	5	0.0603	0.0495
5	8	0.0352	0.0330
6	12	0.0101	0.0224
7	16	0.0000	0.0165
8	20	0.0000	0.0118
9	25	0.0000	0.0082
10	30	0.0000	0.0059
11	40	0.0000	0.0029
12	50	0.0000	0.0018
13	60	0.0000	0.0012
14	70	0.0000	0.0000
15	80	0.0000	0.0000
16	90	0.0000	0.0000
17	100	0.0000	0.0000

3.10. Comparison with the Massey Model

Since there is already a pixel-based CTE correction for ACS’s WFC that has been presented in the literature and made available for users, it is worthwhile to note here the ways in which our approach is similar to and different from that of Massey et al. (2010).

Our approaches are similar in several respects. First, both approaches model the pixel-transfer process, keeping track of the number of electrons in each pixel’s packet, and the number of electrons that get trapped and released in each transfer. We both assume that a trap will grab an electron the instant the trap is open and has an accessible electron to trap. We also both model the trap density as a function of packet intensity, finding that the cumulative number of relevant traps goes roughly as the square root of the amount of charge in the packet.

The first major difference between our models is in terms of the profile of the trails. Rather than fit the trails with hard-coded dual exponentials, our model uses a purely empirical drop-off, parametrizing the 100-pixel trail with 17 nodes, spaced every pixel at smaller offsets and every ten pixels at larger offsets. This flexibility allows us to more accurately tailor the drop-off to the observations. Figure 5 shows that a dual exponential does not adequately describe the entire visible trail.

Another difference is that our treatment deals naturally with variations in the background. One of the variables they invoke in their §2.5, $n_q(y, n_e, b)$, explicitly acknowledges that the background will impact the CTE losses. However, since all of their development data were taken with backgrounds of 51 ± 9 electrons, they were unable to explore this component of their model. They implemented the idea of a “notch” at the bottom of the pixel well that lets through without loss any charge packet with $n_e < 100$ electrons. Since our model was constrained using data with the lowest possible background, we were able to probe the trap density all the way down to the traps that affect even small

electron packets. We find that, rather than dropping to zero at $n_e < 100$ as their model stipulates, the trap density actually continues to increase below this fill-level⁴. The main impact of increasing the background is to pre-fill and take out-of-play the lowest charge traps. As such, we anticipate that our algorithm should work with all kinds of backgrounds, not only those brighter than 51 electrons. This claim will be explicitly evaluated in §3.11.

The third major difference between our models concerns how traps are simulated. Massey et al. (2010) simulated placing explicit traps that affect single electrons at random locations within the pixel grid. While they experimented with making more traps that could affect partial electrons, or fewer traps that would each affect multiple electrons, at heart their treatment was a quantized treatment of the traps. Each of their traps was also thresholded to affect electron packets at specific charge level. Neither the placement of the traps nor their thresholds were empirically determined to match the detectors, but were simply one possible realization of the detailed detector based on their model. Our treatment, on the other hand, deals with traps in a continuum sense. Whereas they modeled about half the pixels as having a trap of one variety or another, we modeled *all* pixels as having an array of fractional traps that affect packets from $q = 1$ to 40,000 DN₂. Consistent with our continuous approach, we find for an observed 2-byte-integer pixel array with a quantized number of electrons a 4-byte-real source array, which can have fractional electrons, and which essentially represents the expectation value for how many electrons

⁴ The WFC detectors were manufactured to have a “notch” or “mini-channel”, so that the smallest charge packets could be transferred with significantly less CTE loss. Unfortunately, the doping did not stay in the small channel but dispersed into the rest of the silicon lattice, thus resulting in no trap-free channel. Manufacturing procedures have improved considerably since the ACS chips were made. (ACS Technical lead, D. Golimowski, personal communication).

were most likely present before the charge-smearing readout process.

A final difference is that we found the need to iterate more than once, whereas they determined a single iteration to be sufficient. We found that only after 3 or so iterations did the modeled and observed pixel arrays converge. We generally iterate 5 times. Perhaps our need for more iteration is related to the more continuous way we modeled the traps. It could also be related to the fact that we are working with a stack of 168 images, and the noise threshold is much lower.

3.11. Examining WPs on different backgrounds

The low background in the dark exposures allowed us to detect the very faint trails behind very low warm pixels. We cannot, however, use these dark images to test the algorithm on more typical science images, which tend to have backgrounds between 20 and 150 electrons (10 and 75 DN₂). The tests we ran with CRs (see Figure 7) seem to validate the assumptions that our model makes in regards to shadowing, namely, that a trap will absorb an electron the instant it can. Electrons in the sky background should work in a way similar to the leading pixels in the cosmic rays we studied: they should pre-fill some traps, so that the upstream charge is subject only to the traps that are above the background level. However, this needs to be empirically verified.

We examined three different F606W images taken of the 47 Tuc calibration field with exposure times of 30 s, 150 s, and 350 s, and with backgrounds of 1.5, 8, and 16 DN₂. We applied our CTE-restoration scheme to each of the `_raw` exposures to produce a corrected raw image and used the warm-pixel locations identified from the peak-map of our previous study. We then examined the WP profiles in the original and corrected images. Since these results come from individual exposures, rather than the dark stack of 168 exposures, we

would naturally expect things to be much noisier, even if the general trends are corrected.

Figure 12 shows the results in an array of panels, for warm pixels with intensities of 15, 50, and 100 DN. We could not cross-compare brighter WPs, since the short 15 s exposures allowed few warm pixels to get very bright. It is illustrative to compare the trends across rows. On the left, where the background is lower, the observed trails are clearly larger than on the right, where the background is higher. This effect is almost a factor of 3 for the faintest WPs, and a factor of 1.5 for WPs with ~ 100 DN₂.

The corrections do a good job for all cases, naturally tracking the disparate CTE impact with background. In most cases, the flux in the trail is reduced by well over 90%.

This first set of tests on the background is encouraging. It tells us that our algorithm properly accounts for the shadowing that results as the background pre-fills traps. This, in turn, results in less CTE loss for faint objects. The next tests will involve studying how the algorithm works for stars, which are more complicated than the delta-function-like WPs. Also, since we know the true fluxes, positions, and shapes for stars, we can assess our correction in an absolute sense.

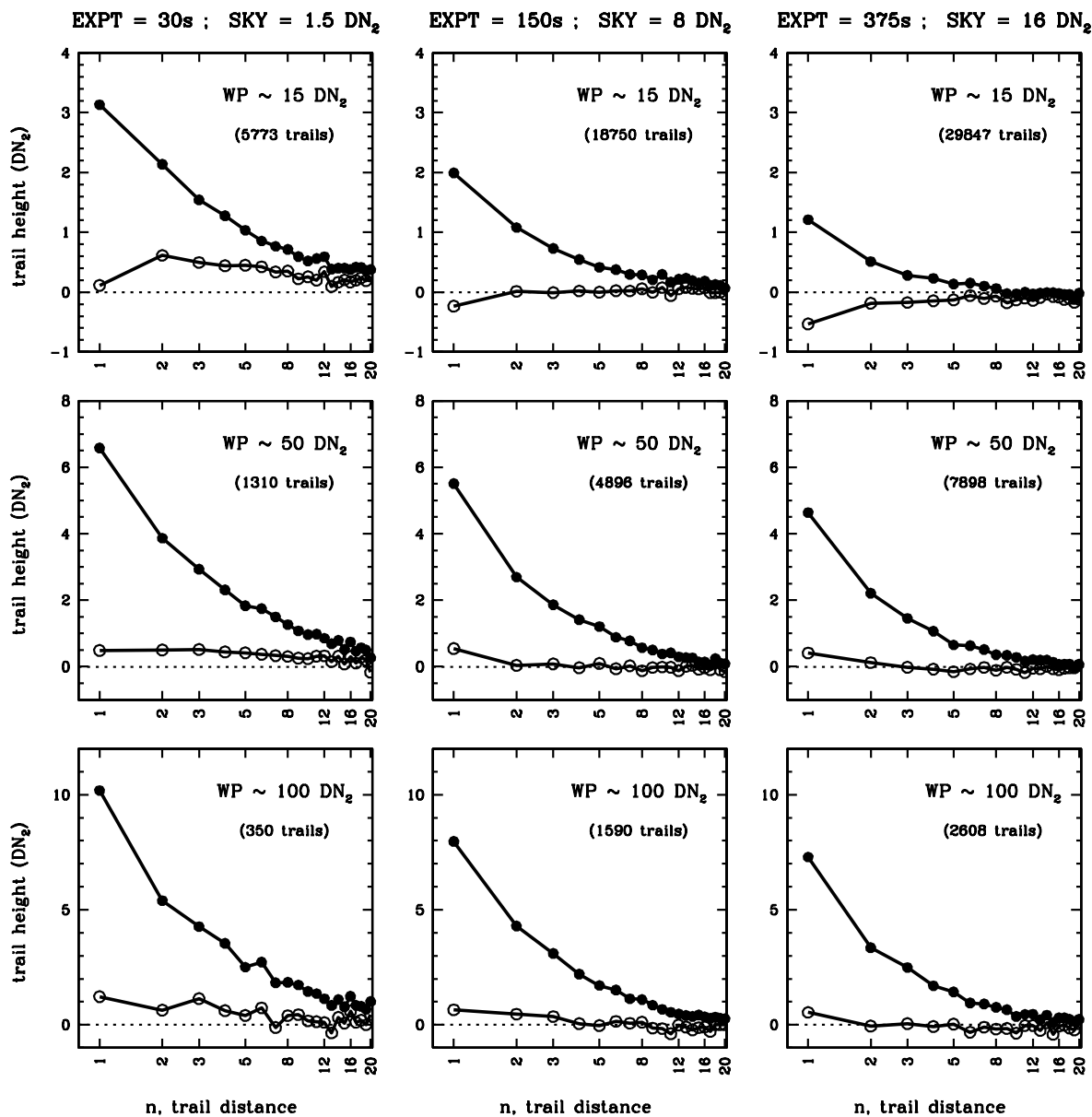


Fig. 12.— The CTE trail profiles for warm pixels in the original and corrected `raw` images of the 47 Tuc calibration field. The curve with the filled symbols represents the raw, observed trails. The open-symbol curve represents the trails in the corrected exposures. The panels on the left show 30 s exposures with a background of only 1.5 DN_2 , the middle panels show the results for 150 s exposures, with a background of 8 DN_2 , and the right panels show 375 s exposures with a background of 16 DN_2 . In each column, the panels from top to bottom show the results for faint to moderate warm pixels.

4. TESTING WITH STARS

The restoration of charge into the delta-function-like warm pixels is a basic test that any pixel-based algorithm should pass. This test is a necessary—but not a sufficient—demonstration that the algorithm is robust for science images. It is possible that there could be some species of traps that release the charge over much longer time-scales (and hence, longer trail distances) than can be measured with even bright sources. Such traps would leave no perceptible trail, yet they could still remove significant charge from objects.

The only way to test whether our algorithm actually does restore all the lost flux is by comparing various restored images against the truth. This can be done in two ways. In the first test, a shallow-exposure image can be corrected and compared against a corrected deep-exposure image. Since the CTE losses for the the first exposure would be much larger than for the second (thanks to the higher background in the second), the comparison provides a direct empirical test. This comparison could involve extracted parameters such as fluxes or positions, or it could be made on a pixel-by-pixel basis. The second test will involve comparing two images that are dithered vertically by a whole chip, which maximally enhances the CTE contrast.

Before embarking on these tests, however, we should perform the æsthetic test. Does it *look* like the trails have been removed in science images?

4.1. Removal of Trails from stars

In the panels of Figure 13, we show the uncorrected, corrected, and difference images for two exposures of the 47 Tuc calibration field: `ja9bw2ykq_raw`, which had an exposure time of 30 s and a low background (1.5 DN₂, top) and `ja9bw2y1q_raw`, which had an exposure time of 349 s and a higher background (16 DN₂). In both cases, the CTE trails

from stars are obvious in the original images on the left, and are indiscernible in the corrected images in the central panels. The difference images show how the correction algorithm has redistributed the flux.

The scaling for the image panels has been matched to the exposure time, so that the more significant corrections in the upper-right panel, as compared against the lower-right panel, indicate a much larger fractional adjustment for the lower-background images.

It is worth noting that many of the CRs in the short exposure in the top panels have their trails over-subtracted, while this does not appear to be the case for the 349 s exposure. The reason for this is that the detector is not read out instantaneously. The read-out takes about 100 s seconds (see §2.1) and the pixels in these short exposures thus spend more time getting read out than they do exposing on-sky. Consequently, it is more likely than not that an observed CR will have struck the detector during readout, rather than during the formal exposure time. As such, this late-hitting CR will not have been transferred across the entire array, but only part of it, and the correction, which assumes j pixel-shifts for an object appearing in row j , will naturally over-correct.

The fact that the corrections developed to remove the CTE trails from warm pixels also appear to do a good job restoring flux to stars is a good sign that the algorithm has universal application. The real test, however, will involve a more quantitative analysis.

4.2. Testing the algorithm on `_flt` images

The raw corrections in the preceding sections were performed on the `raw` images, which have not gone through the standard pipeline process of bias-subtraction and flat-fielding. It is worth asking whether it would be safe to work with the `flt` exposures, instead. It would certainly be easier if the algorithm could operate on pipeline products, so that it would not

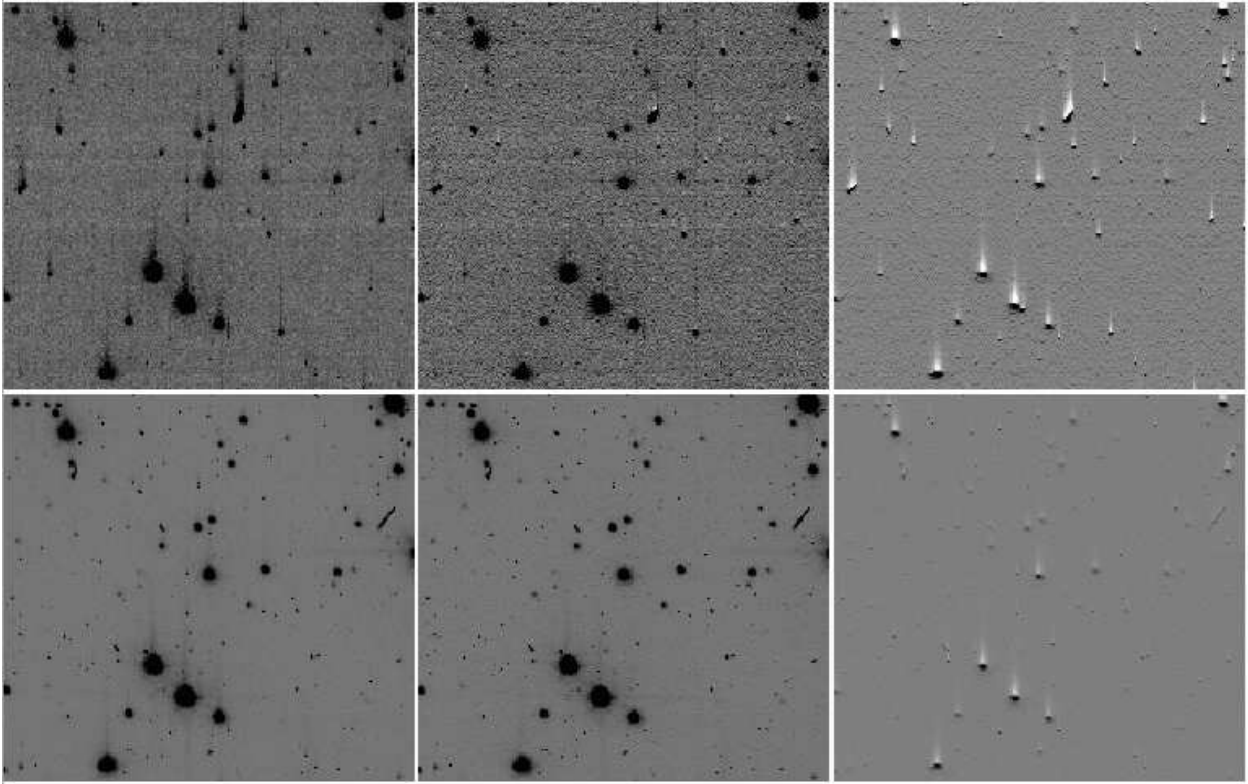


Fig. 13.— Panels from left to right show, respectively, the original **raw** image, the corrected **raw** image, and the difference between the two. The top panels show the results for **ja9bw2yq** a 30 s exposure, and the bottom panels show them for **ja9bw21q**, a 349 s exposure.

be necessary to re-run the pipeline calibrations by hand afterwards⁵.

To test this shortcut, we first divided the `flt` images by two to account for the fact that the `flt` images are in electrons, while the corrections were developed for the `_raw` images, which represent DN with a gain of 2. We then ran them through the same procedure as above, and multiplied the output by 2, to restore the scaling back to electrons.

The resulting images look extremely good; the trails appear to be removed nicely, just as well as in the raw images. This makes sense in that the flat-field process should not introduce much more than a 5% adjustment in the value of a pixel (the relative correction is typically less than 2%). While the CTE losses are not perfectly linear with pixel value, over a small range they are nearly linear, so it makes sense that operation on the `_flt` images would be nearly the same as on the `_raw` images. In the remainder of this section, we make use of the `_flt`-stage routines to evaluate the efficacy of our correction in terms of absolute flux, astrometry, and shape. As such, we will be reporting the results in electrons, not DN₂.

4.3. Shallow-vs-Deep tests

It is well known that imperfect CTE affects short exposures with low background more than long exposures with higher background, so to test our correction we compared the short-exposure photometry and astrometry against the long-exposure photometry and astrometry. Cycle-17 Program GO-11677 (PI-Richer, Co-I Anderson) will spend a total of 121 orbits staring with ACS at the outer calibration field in 47 Tuc, with the aim of detecting the end of the white-dwarf cooling sequence. As of this writing, 18 out of 24 visits

⁵ If, in the end, this correction is deemed to be valid, it may be worthwhile to revisit some of the pipeline files, such as biases and darks, to see how they may have been affected by imperfect CTE. However, we will defer that discussion until Section 6.

have been successfully taken. The observations in hand were taken in F606W and F814W, with exposure times typically between 1200 and 1300 s, depending on the visibility. A single short exposure of 1 s, 10 s, or 100 s was taken at the beginning of each visit. Each of these short exposures was followed immediately by a very deep exposure at the same pointing through the same filter, which will allow us to compare the CTE impact on the shorts and deeps. The 1 s images did not have enough bright sources that could be seen unsaturated in the deep images to be useful, so we focus below on the 10 s and 100 s short exposures. For reference, the 10 s exposures have a background of about $2 e^-$ and the background in the 100 s exposure was about $15 e^-$.

We took the three 10 s and the three 100 s short F606W exposures and their deep counterparts and corrected them for CTE according to the algorithm described above. We ran the routine `img2xym_WFC.09x10`, which is described in Anderson & King (2006), on the uncorrected and corrected `_flt` images. This software program measures fluxes and positions for stars in individual exposures by fitting an empirical library PSF to the central 5×5 pixels for each star. The photometry it produces is equivalent to aperture photometry over the fitting box, with a correction for the fraction of the PSF that should have landed in the box, given the measured position of the star within the central pixel of the box.

By comparing the 10 s and 100 s images against their deep counterparts, we can examine directly how well our correction mitigates CTE in both astrometry and photometry. Figure 14 shows the results from comparing the 10 s images against the ~ 1200 s images for before and after CTE correction. Figure 15 shows the same comparisons for the 100 s images.

The left column of panels of Figure 14 shows the photometric residuals for the 10s-vs-deep comparison. The vertical scale covers ± 0.75 magnitudes in flux. All the pre-correction comparisons show very significant CTE impact, with the familiar bow-shaped

residuals indicating that stars at the center of the abutted two-chip system are farthest from the serial register and suffer more CTE loss in the short exposures than in the deep exposures. The upper-right panel shows that the brightest stars, with an instrumental magnitude⁶ of -8 , suffer a loss of about 0.2 magnitudes (20%). The lower-right panel shows that the faintest stars at $m \sim -4$ suffer a loss of almost a 50%. Yet, in both cases the algorithm restores the photometry nicely, with an error generally less than 10% of the correction itself.

The left panels of Figure 15 show the same for the 100 s exposures. Stars in these medium-length exposures exhibit about a factor of two less CTE than stars of a similar brightness in the short exposures.

The panels on the right of both figures show the astrometric residuals along the readout direction (y). Since the images were taken immediately after one another with the same guide stars, they should be almost perfectly co-registered. The third column of plots exhibits the telltale sign of astrometric CTE (see Kozhurina-Platais et al. 2007): stars nearest the inter-chip gaps are farthest from the serial register and suffer CTE that shifts their position in the direction of the gaps. The fourth column shows the corrected residuals, which largely remove the CTE signature. Some of the intermediate-brightness objects in the 100 s exposures appear to be slightly over-corrected, but even there the correction is better than 75%.

It is worth noting that we originally made this comparison using the corrected short exposures and the uncorrected deep exposures, thinking naïvely that the deep exposures with their background of over 100 e^- essentially made them immune to CTE losses. We found that without correcting the deep exposures as well, the short-vs-deep residuals

⁶ Instrumental magnitude is defined as $-2.5 \log_{10}(FLUX)$.

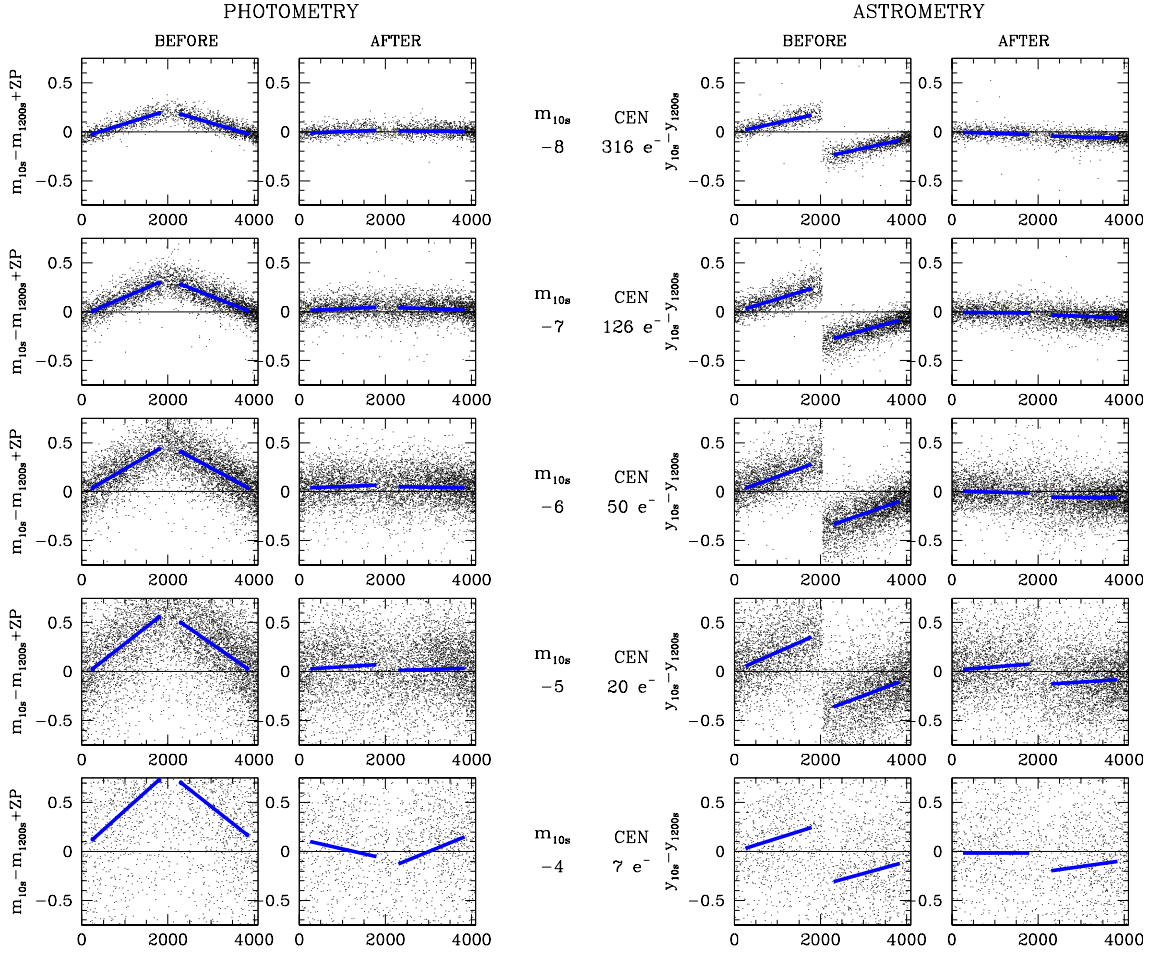


Fig. 14.— Comparison of photometry and astrometry between 10 s and 1200 s images for uncorrected and corrected images. The photometric comparison is shown on the left, and the astrometric comparison on the right. Photometry from the deep exposure has been zero-pointed to correspond to the short exposure. The residuals are plotted against the raw y coordinate in a system that has the two chips abutted at $y = 2048$. The different rows of panels show the residuals for stars with different short-exposure instrumental magnitudes. Stars brighter than -8.5 in the 10 s exposures are saturated in the 1200 s exposures, so they could not be included. The central column lists the instrumental magnitude and the corresponding central-pixel intensity. The blue lines represent a linear fit for the trend against y .

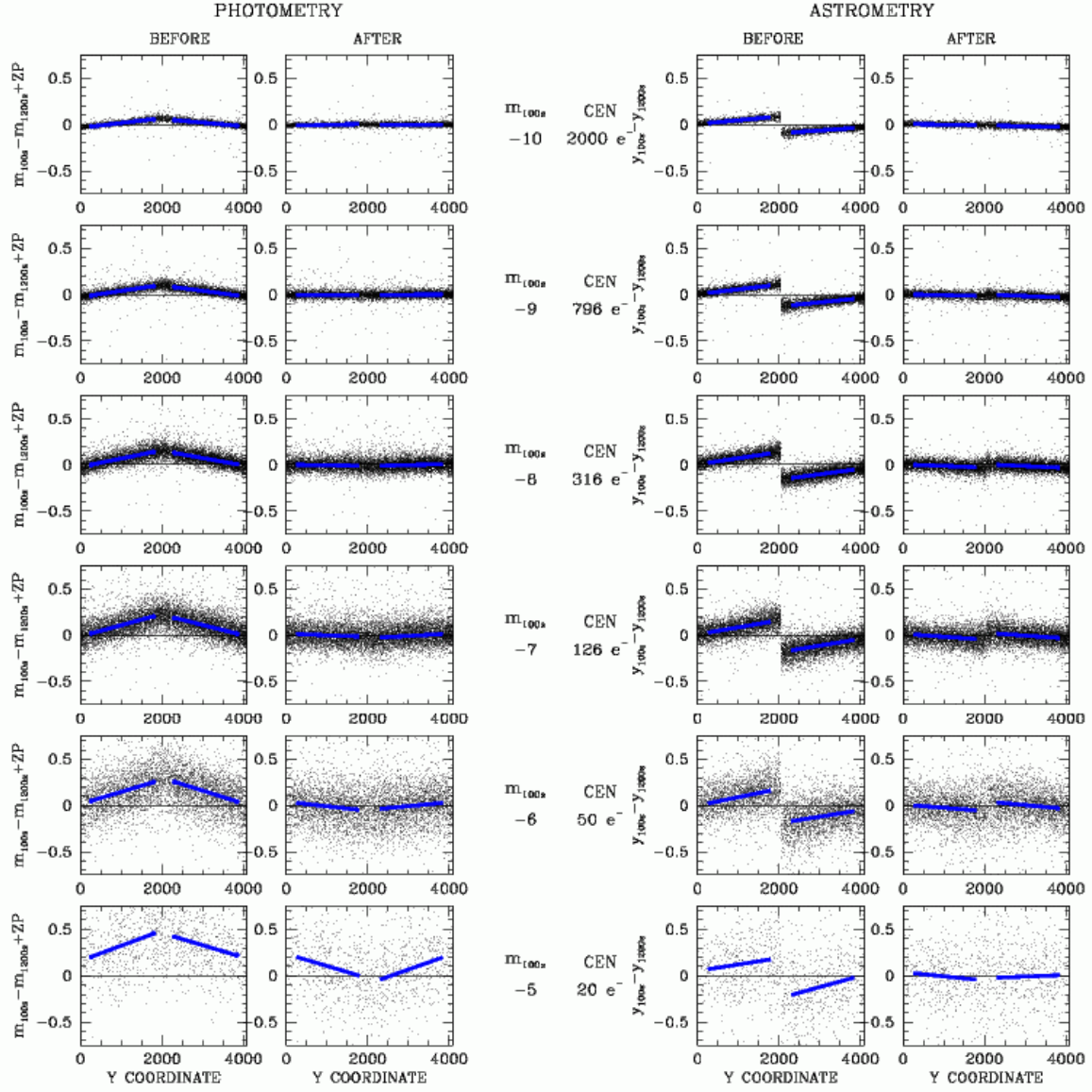


Fig. 15.— Same as Figure 14, but this time comparing the 100 s and 1200 s exposures. Stars brighter than -10.5 in the 100 s exposures are saturated in the deep exposures.

indicated that the algorithm appeared to be over-correcting the short exposures. However, when we applied the correction to both exposures, the correction was seen to be accurate and clearly relevant for both short and deep exposures, as seen in Figures 14 and 15.

The fact that our correction restores photometry as well as astrometry is an indication that the flux we have associated with the trails is indeed almost *all* of the flux that is delayed by traps. This was not an assumption of our algorithm; the aim of the algorithm was simply to restore the perceptible flux. The fact that it appears to restore almost all the flux is satisfying. This results is in contrast to what has been seen with WFPC2, where trail-based CTE corrections were deemed inadequate because they clearly did not account for all of the flux (see Figure 7 in Cawley et al 2001). Of course the trail shapes and time constants can be very different for ACS/WFC and WFPC2, with their different array sizes, dopings, temperatures, and parallel-readout cadence. It should not be surprising that they would have different trail profiles, and that WFPC2 with its faster readout (13 s vs 90 s) might have longer trails in a pixel sense. We do note, though, that some investigations have shown that if the WFPC2 trails are modeled out to 90 pixels, the lost flux is in fact mostly accounted for (Biretta & Platais 2005).

Laboratory FPR (first-pixel response) and EPER (extended pixel-edge response) tests have suggested that the observable trails do not contain all the flux. However, such tests generally involve reading out only 20 or so virtual pixels, so they can measure the the flux only in the inner part of the trail. Our trails have perceptible flux out to 60 pixels, so the conclusions from traditional EPER tests are not directly relevant. Waczynski et al. (2001) made the same point, and found that when in their lab experiments they extended their EPER test to 200 or 900 overscan pixels, they recovered the flux implied by the FPR tests.

In Figure 16 we compare the amplitude of our corrections against those predicted by Chiaberge et al. (2009), plugging in for the date and background of our exposures. The

aperture we used is effectively 2.8 pixels in radius, slightly smaller than the 3-pixel-radius of the Chiaberge correction, but the results should not be particularly sensitive to this. The upper panels show our net correction and the Chiaberge correction for the 10 s and 100 s data set, as well as the trend seen in our correction. The agreement is better than 20% everywhere, and is additional encouragement that our correction restores essentially all of the flux. The error bars drawn on our points reflect the photometric spread about the mean, not the error in the correction. The bottom panels of the figure show the astrometric residuals, for which no Chiaberge-type empirical correction exists.

4.4. The offset-image test

The ACS team regularly takes images to trend CTE losses. One such program involves imaging the 47 Tuc calibration field with one pointing, then shifting the field vertically by one WFC chip so that the stars on the top chip in one exposure will be on the bottom chip in the other. Such a strategy magnifies the impact of CTE, since stars farthest from the readout in one exposure will be closest in the other.

We have examined two such pairs of 30 s images taken in June 2009 soon after SM4: ja9702sxq, ja9702szq, ja9702t5q and ja9702t7q. The images have a background of about $4 e^-$. We measured the stars in all the exposures (corrected and uncorrected) using the same photometry routine as above, and compared the photometry for stars found in all four exposures as a function of where the star was found in the bottom-chip exposure.

The results of this test are shown in Figure 17. The size of the effect here should essentially be twice that seen in a single exposure. We see that before corrections, the relatively bright stars that are farthest from the amplifier in one exposure and closest to it in the other differ by 12.8% (i.e., 2×0.064). The fainter stars differ by more than 50%.

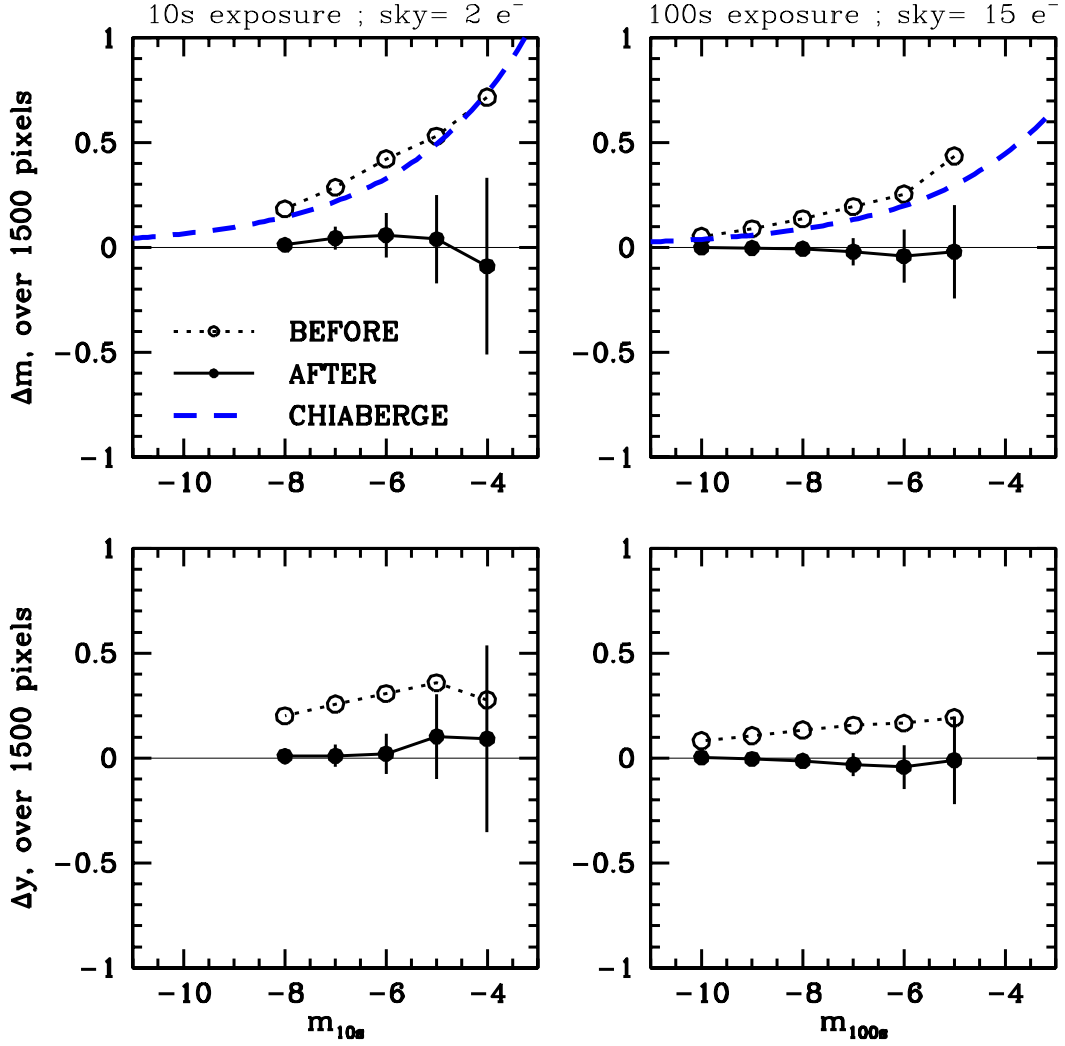


Fig. 16.— The net photometric and astrometric corrections from our algorithm, in the upper and lower panels, respectively. The photometric corrections are compared against the Chiaberge et al. (2009) correction for the appropriate date and background level. The error bars indicate the spread in the residuals, not the error in the correction.

After the corrections, there is very little discernible trend.

4.5. More absolute tests

We have also looked into more “absolute” tests, and compared positions measured in individual exposures of the 47 Tuc calibration field against photometry and astrometry in a reference catalog that has been constructed from many pre-SM4 exposures taken at a variety of orientations and offsets. The photometric results were very encouraging, but not perfect, perhaps indicating that the reference catalog has been compromised more than anticipated by CTE. In an astrometric sense, the stars in the reference frame are all moving with internal motions of about 0.5 mas/yr relative to each other due to the cluster’s internal motion (McLaughlin et al. 2006), making the astrometric handle fuzzy.

Over the next few months, as this routine is evaluated for use before SM4 and before the temperature change, we will apply it to the archive exposures and construct a better catalog, which can provide a photometric “truth” against which observations can be compared directly. Also, the GO-11677 data set will be ideal for examining the CTE correction and its efficacy for faint sources on moderate backgrounds.

4.6. Comparing shape

The fact that the astrometric bias is generally removed by the CTE correction encourages us to think that the correction might preserve shape as well. This aspect of the correction will be important for studies of lensing and galaxy morphology. We study this more quantitatively by examining the profiles of stars in the corrected and uncorrected deep and shallow images.

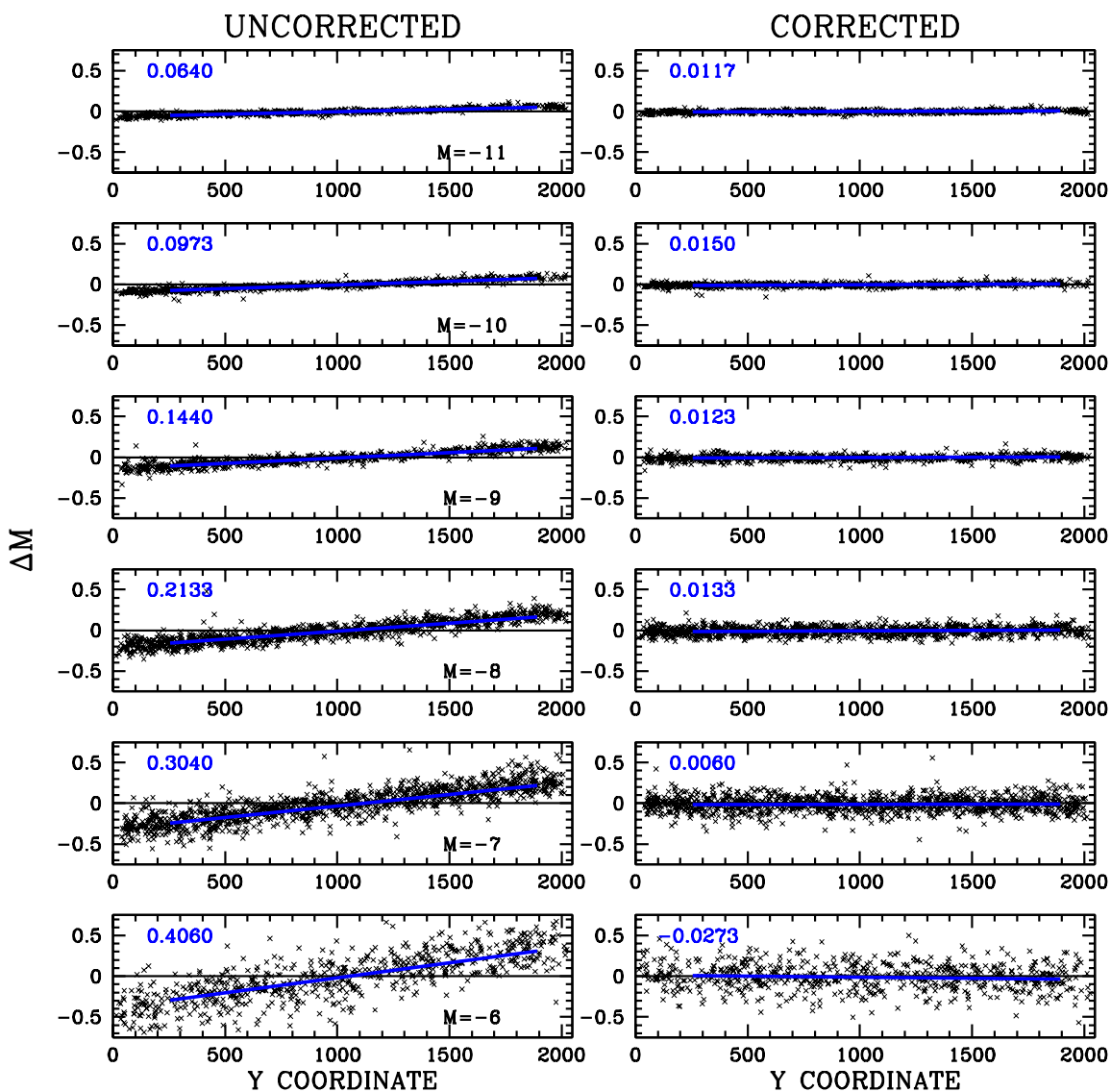


Fig. 17.— Comparison of the measured brightnesses of stars in images that have been shifted by a full chip to enhance CTE impact. Uncorrected images are shown on the left, and corrected images on the right. The panels from top to bottom shows stars with: 25000, 10000, 4000, 1500, 630, and 250 e^- total flux. The blue lines indicate the linear trend, and this slope (divided by two, to account for the two-image comparison) is indicated in the upper left of each panel.

We began by mapping the star catalog from Anderson (2007) into the `_flt` frames of `ja9bw2ykq` and `ja9bw2y1q`, which had exposure times of 30 s and 339 s and backgrounds of 3 and 35 e^- , respectively, and were taken immediately one after the other with no dither offset. We analyze only the stars between $y = 1500$ and $y = 2000$ of the bottom chip in an effort to maximize our sensitivity to CTE-related issues.

The catalog was constructed in 2005. Using the exact 2005 positions in 2009 images would introduce proper-motion-displacement errors to our positions, so we used the catalog only to identify *bone fide* stars. We used the library PSFs described in Anderson & King (2006) to determine an improved position and flux for each star in the deep corrected image. We then extracted a 5×5 raster centered on each star from each of the four images (the corrected and uncorrected deep and shallow exposures). We also removed from each raster a sky as measured from the annulus between 8 and 12 pixels. Finally, we examined these pixels to see how imperfect CTE had modified the stellar profiles, and to determine whether our corrections had restored them.

Anderson & King (2000) showed how one can directly examine the PSF profiles of stars if we have an estimate of their fluxes and positions (see their Figure 6 and Eqn. 7). From the deep corrected exposures, we have estimates of the stars' positions and fluxes, so we can examine their profiles. In Figure 18 we plot the vertical profile of the central part of the PSF for stars of different brightness in the different images. Specifically, we plot $\hat{\psi}(\Delta x, \Delta y)$ against Δy for $|\Delta x| < 0.5$.

The PSF as formulated here simply maps the fraction of light that falls in each pixel as a function of where the pixel is relative to the center of the star. For example, $\psi(0, 0)$ represents the fraction of light that would fall in a pixel when the star is centered on that pixel. For the WFC PSF in F606W, between 19% and 25% of the light in the star falls in the central pixel (Anderson & King 2006).

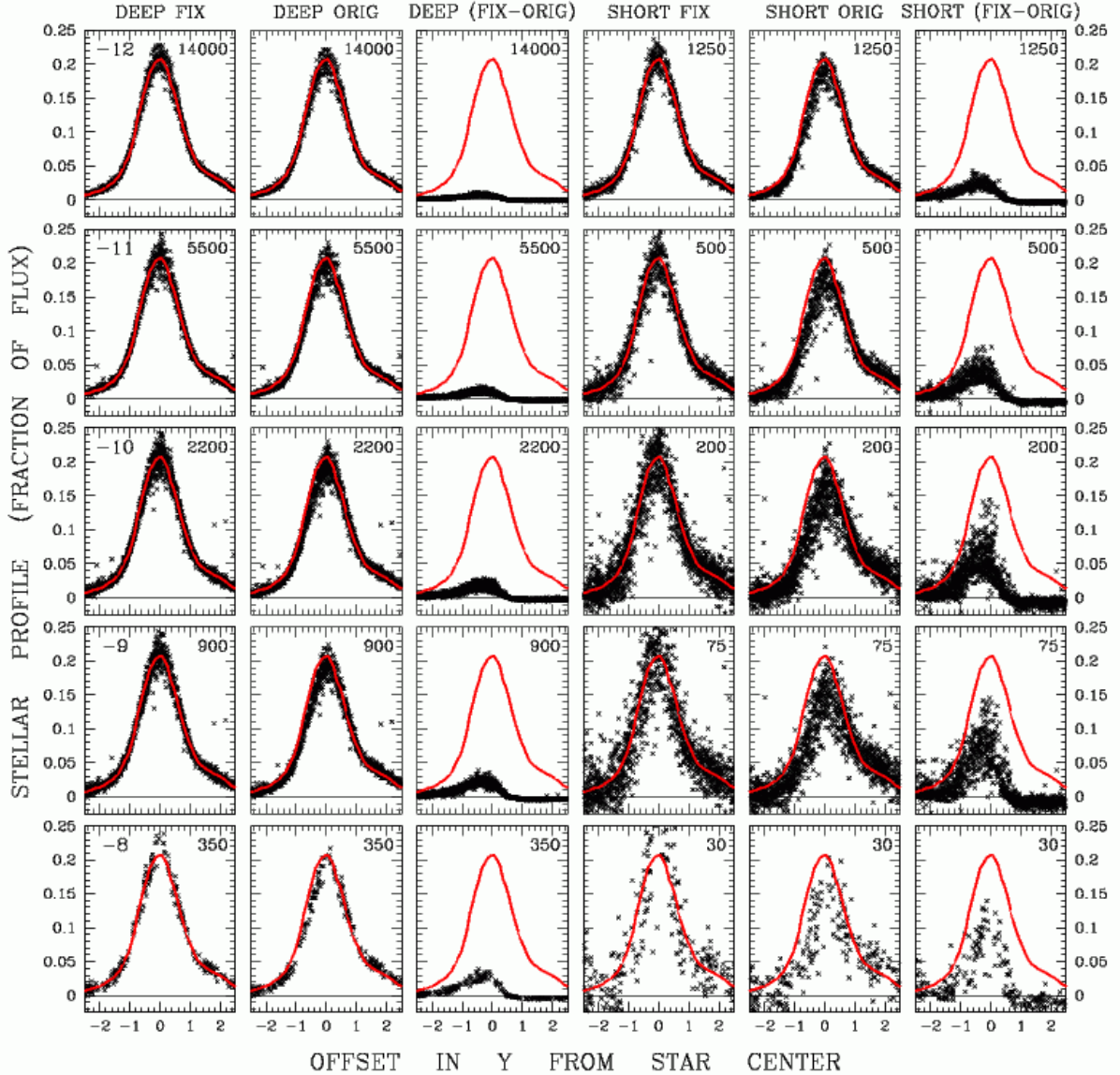


Fig. 18.— The profiles of stars in corrected and uncorrected deep (339 s) and short (30 s) images of the 47 Tuc calibration field. The first and second columns show the corrected and uncorrected deep exposures. The third column shows the difference, which corresponds directly to the CTE correction. The next three columns show the same, but for the shallow exposure. The brightest stars are shown in the top row, and the faintest in the bottom row, with the deep-image instrumental magnitude listed in the upper left of the left plots. The flux in the central pixel of a typical star is listed (in e^-) in the upper right of each panel. The PSF profile (red solid line) drawn in each plot comes from tracing the distribution in the upper-left panel, and reproducing the same curve in the other panels. The units of the vertical axis are fraction of flux in each pixel, relative to the total within a $0.5''$ aperture.

All stars bright and faint should have the same PSF (leaving aside issues of minor position-dependent variations). The upper-left panel shows the profile for the brightest stars in the corrected deep image. This should be representative of the true PSF profile, so we trace it with a red line and plot it for reference in all the other panels. Going down, we show that the stars from instrumental magnitude -12 to -8 in the corrected image all have the same profile, in that the points (each of which represents one pixel in one star image) all trace out the same curve. The brightest stars have $14000 e^-$ in their central pixels, and the faintest have $350 e^-$. All the panels in each row show the exact same stars.

The next column over shows the profiles from the untouched deep exposure. This by and large traces the same profile, but as the source gets fainter, it is clear that the leading edge (on the left) suffers some CTE losses. The third panel shows the difference between the two profiles, corresponding directly to the adjustment that the CTE algorithm has made to the original pixel values.

The fourth panel shows the profiles from the stars in the corrected short exposures. The brightest stars here have $1250 e^-$ in their central pixels and the faintest have only about $30 e^-$. It is clear that the corrected pixels follow the profiles extremely closely—even for the faintest stars. Our correction not only restores the flux but also the shape of astronomical sources.

The second to last column shows results for the untouched short exposure. It is easy to see here how imperfect CTE has shifted and modified the stellar profile: a larger and larger fraction of electrons from the leading edge of the star are lost as the star gets fainter. By contrast, there is a clear excess of flux in the CTE trail on the right.

The adjustment made by our algorithm is shown in the rightmost column. The faintest stars require an adjustment that corresponds to nearly 50% of the original flux.

Our CTE restoration algorithm was constructed entirely from the profiles of warm pixels in dark exposures, with no reference whatsoever to stars or their profiles. The fact that this algorithm restores the pixels of a stellar profile to their rightful values is a clear independent demonstration that the algorithm not only corrects stars' fluxes, as we saw in §4.4, but puts the flux in the right place as well. This gives us every reason to think that the same should be true for resolved galaxies, which are even less sharp than PSFs.

5. POSSIBLE IMPROVEMENTS TO THE ALGORITHM

The preceding sections have shown that our CTE-correction algorithm clearly works quite well. The process of restoring flux to the bright sources naturally lowers and improves the uniformity of the background as well. This can be seen from a simple inspection of the images. However, there are still some remaining issues, such as: read-noise amplification, the speed of the algorithm, and CTE issues in the serial direction. We will address these below.

5.1. Readnoise Amplification

The imperfect charge-transfer process tends to blur out the images. What is originally a delta-function warm pixel gets read out as a less intense delta function with a tail. In general, this blurring will be mild. If we have a single bright pixel with more than 15 DN_2 on a negligible background, most of the electrons will stay with the original pixel packet, and we can hope to re-associate the trail-electrons with their original packet.

Nevertheless, the reconstruction process still constitutes a deconvolution, however mild, and as such it should be expected that a reconstructed image will end up being sharper than the image that was read out at the amplifier. Therefore, to the extent that the observed

image has any variation from pixel to pixel, the reconstructed image will necessarily have more. So long as this ends up restoring true lost sharpness to stellar profiles or object morphology, this sharpening is appropriate. But there is one component of the observed image that did not participate in the charge-transfer process: the read-out noise (RON).

The RON in ACS was $5.5 e^-$ before SM4 and has been 3.9 to $4.7 e^-$ since SM4 (Maybhate et al. 2010). This noise gets added to the image pixels as they are read out at the amplifier. It was not present during the pixel transfer, so if we invert the readout process on an image with RON, we will arrive at an image with a scaled-up version of the readnoise, since this is the only way to arrive at the observed image after the blurring readout process. To estimate this amplification factor, we generated an image with a flat background of 5 DN_2 and a readnoise of 2.25 DN_2 , subjected this image to the readout-inversion process and ended up with an image that had a pixel-to-pixel noise of 3.06 DN_2 , thus increasing the readnoise by about 40%. This is not desirable, but it would seem unavoidable, as we would like to neither remove the unavoidable noise arbitrarily, nor amplify it.

Although it is never possible to know precisely what pixel-to-pixel variation in an image is due to readnoise, Poisson noise, or actual structure in the scene, it is possible to take a conservative approach: we will attribute as much of the pixel-to-pixel variation as possible to readnoise and operate our procedure on the rest. To do this, we will separate the observed image I_{OBS} into two components $I_{\text{OBS}} = I_{\text{SM}} + I_{\text{RON}}$. The first component is a slightly smoother version of the observed image; the second component is an image that is consistent with being pure readnoise. As such, it has no large-scale structure with only high-frequency pixel-to-pixel variations with an amplitude of ($< 5 \text{ DN}_2$).

We effected this separation by first taking the original image and smoothing it with a 3-pixel boxcar in y . We subtract this smooth image from the original to obtain the high-frequency component. Any pixels in this component less than 5 DN_2 are likely to be

indicative of read-noise. High-frequency-component pixels greater than 10 DN_2 are likely due to something other than RON (e.g., Poisson noise, real high-frequency structure in the astronomical scene, a WP, or a CR). So, to get the best estimate of the pure RON component, we map this residual $\delta(i, j)$ into $\Delta(i, j)$, something more reflective of something that is pure readnoise:

$$\Delta = \begin{cases} 0 & : \text{ if } \delta < -10 \\ -10 - \delta & : \text{ if } -10 < \delta < -5 \\ \delta & : \text{ if } -5 < \delta < +5 \\ 10 - \delta & : \text{ if } +5 < \delta < +10 \\ 0 & : \text{ if } \delta > +10 \end{cases} . \quad (4)$$

If $|\delta| < 5$, then the high-frequency component for that pixel is consistent with being entirely readnoise, so $\Delta = \delta$. If $|\delta| > 10$, then it is determined to be something other than readnoise and Δ is set to zero. We taper Δ between these two extremes. Finally, we associate the readnoise image with Δ , $I_{\text{RON}} = \Delta$, and the smoothed image is then simply $I_{\text{SM}} = I_{\text{OBS}} - \Delta$.

We then execute the pixel-restoration procedure on the smoothed image, I_{SM} , to get the corrected-smooth image, I'_{SM} . Once this is constructed, we add back in the readnoise component to get the best estimate of the corrected image, I'_{ORIG} . In this way, we aim to operate the restoration algorithm only on the part of the image that is clearly not readnoise, while at the same time, modifying the ultimate noise properties as little as possible.

To test this algorithm, we took a short 30 s exposure of the 47 Tuc calibration field (j9bw2ykq), which has a background of $3 e^-$ and reconstructed it two ways: (1) we applied the reconstruction routine on the original image, and (2) we applied the reconstruction routine on a smoothed version of the original image, then added in the un-smooth part: $I'_{\text{ORIG}} = I'_{\text{SM}} + I_{\text{RON}}$.

Figure 19 shows a portion of the observed `_flt` image, and its smooth and unsmooth

components. The unsmooth image has a total range of ± 5 , and is zero in regions of real structure (near the locations of stars).

Figure 20 shows the two reconstructions. The original image is shown on the left, with the direct reconstruction in the middle and the smooth-based reconstruction on the right. It is clear that the background is much noisier in the middle exposure than in the original or in the reconstruction on the right.

Figure 21 shows the actual difference between the original image and the two restored images. It is clear that the two have similar effects on the stars, WPs, and CRs, but the direct reconstruction clearly adjusts many more pixels in the background. Figure 22 shows this in histogram form. The restoration acting on the original image increases the pixel-to-pixel variation by about 30%, while the restoration based the smoothed image increases it only by 3%.

This multi-step restoration will make a big difference for images where the background is low, but will make only a small difference in images where the noise is dominated by Poisson photon statistics, since this source of noise *has* participated in the CTE-impacted charge transfer. The algorithm presented here may not be the only one way to address the readnoise-amplification issue, however it does demonstrate that it should be possible to restore CTE-trails without introducing additional unpleasant artifacts.

5.2. Improvements in Computational Speed

The prescription given for the algorithm in §3.4 involves dealing with fractional charge traps at every marginal unit of DN_2 . This means that we need to monitor the state of each of up to 40,000 traps, as the flux is transferred from one pixel to another. When operating on typical images with backgrounds of about 25 DN_2 , the routine takes about an hour on a

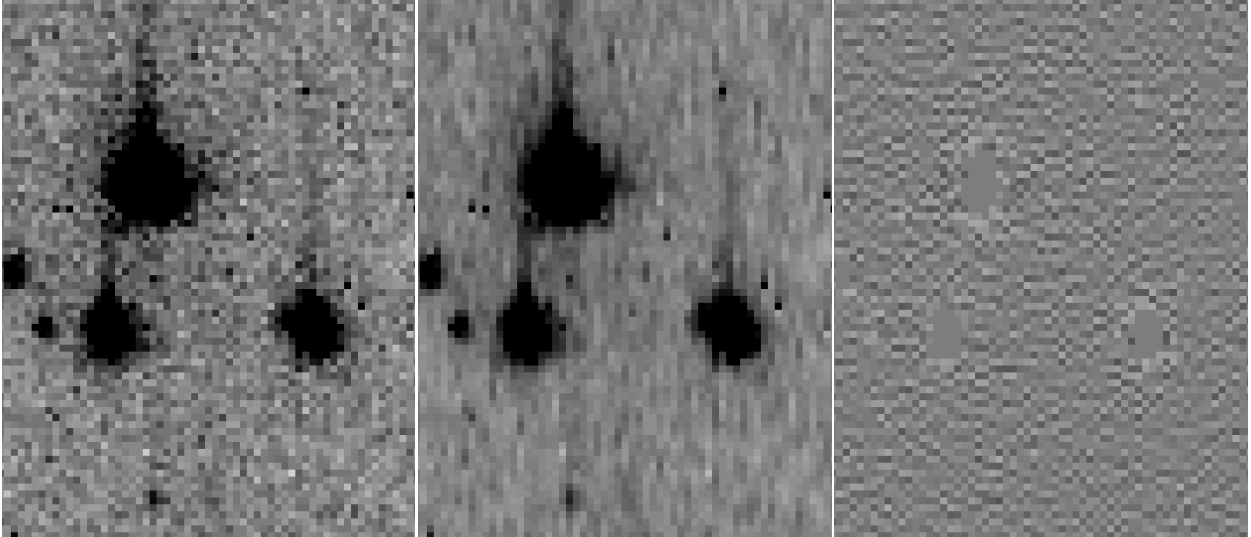


Fig. 19.— (Left) Portion of image `ja9bw2ykq_raw` (background 1.5 DN_2) centered on coordinate (1215,1609) in the bottom chip. (Middle) The smoothed component of this image. (Right) The component of the image attributed to readnoise.

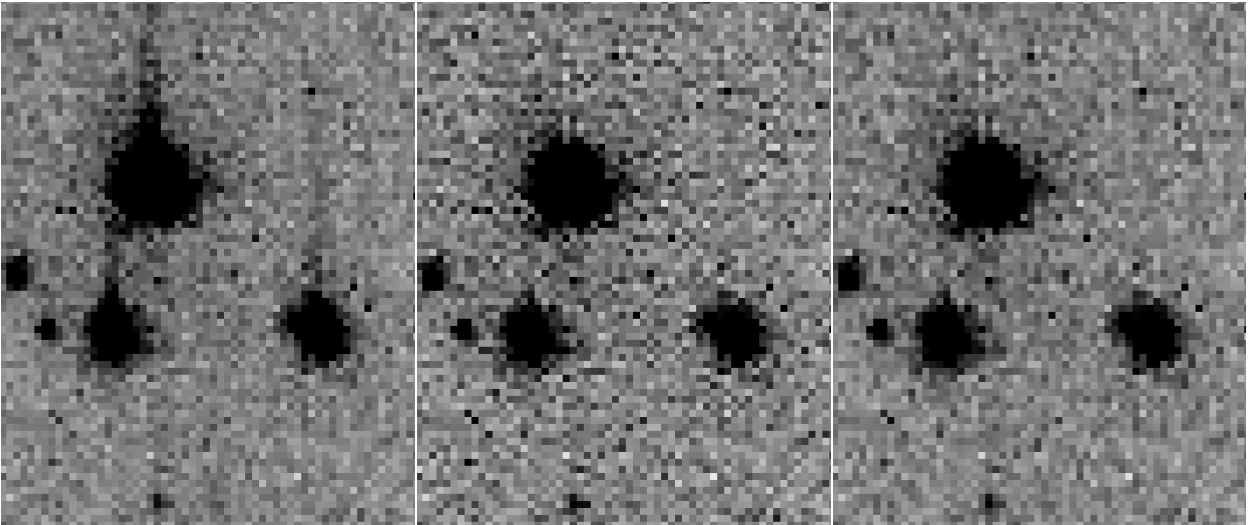


Fig. 20.— (Left) The original image. (Middle) The direct reconstruction of the original. (Right) The reconstruction based on the smoothed image.

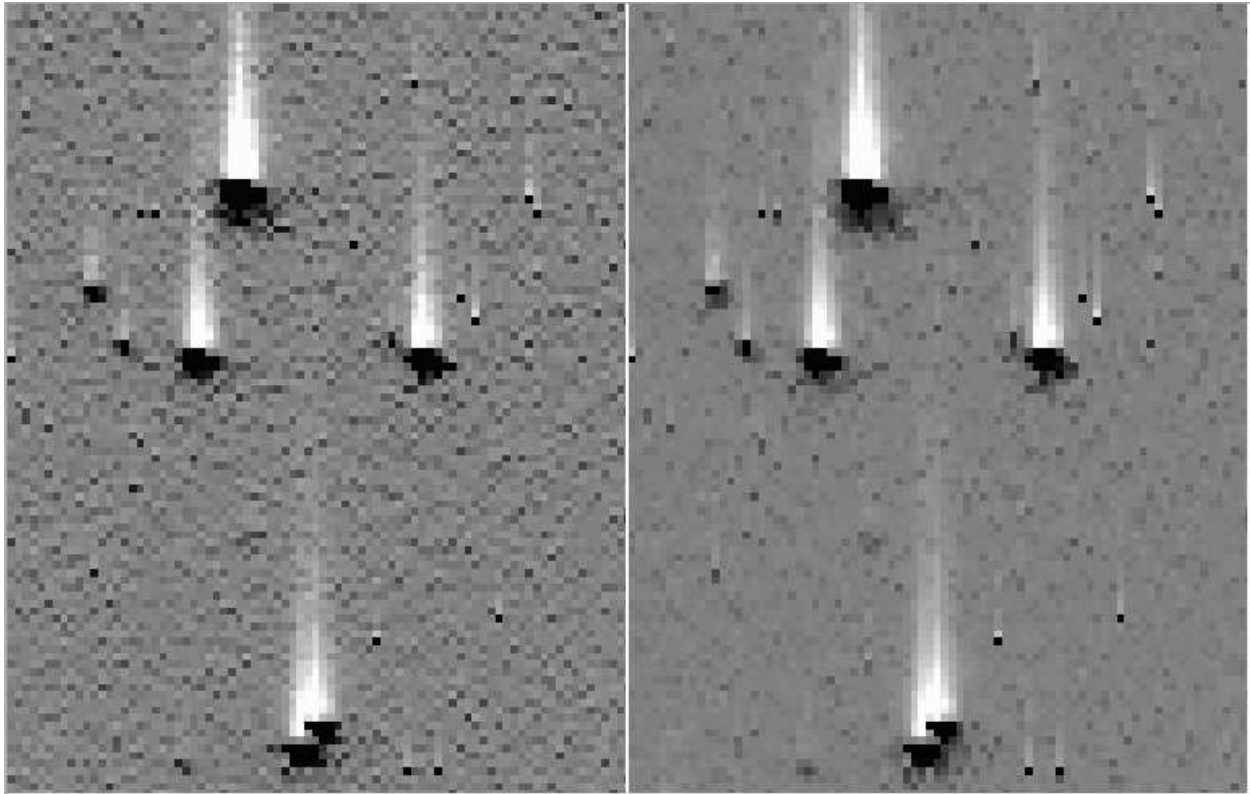


Fig. 21.— The CTE adjustment made to the original image for the direct reconstruction (left) and for the smooth-image-based reconstruction (right).

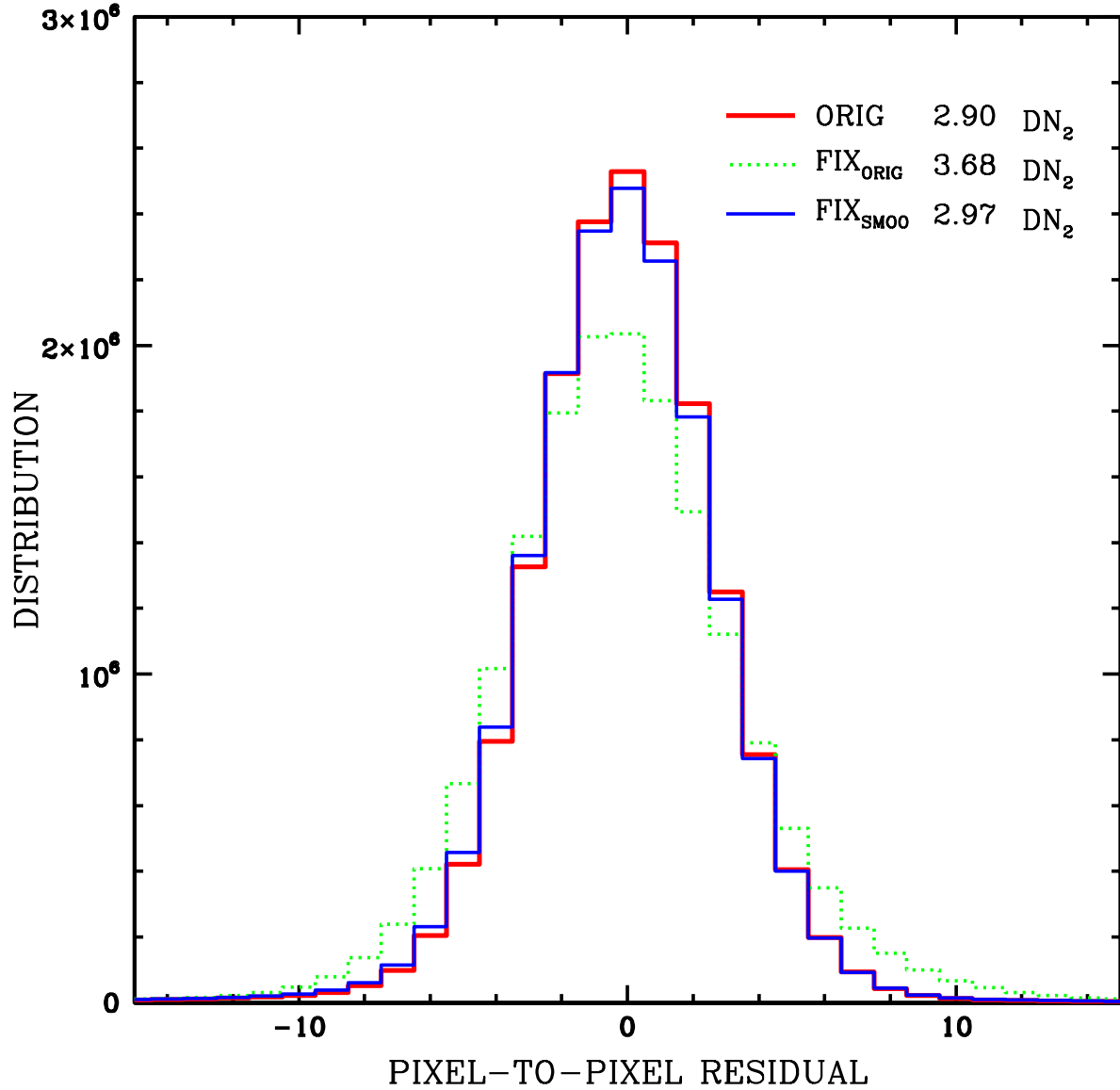


Fig. 22.— Histograms showing the pixel-to-pixel variation in the original image (heavy red), the direct-restored image (dotted green), and the smooth-image-based restoration (blue). The residual is computed for each pixel and is simply the difference between the pixel and the average of its eight surrounding neighbors.

2.4 GHz machine to complete its five reconstruction iterations for all the 4096 columns of both chips. This is not prohibitive, but if it could be sped up without any loss of accuracy, it would be a tangible benefit.

The function ϕ_q tells us how much charge the trap at each DN_2 level (q) can affect. Adding ϕ_q up from $q = 1 \text{ DN}_2$ to $q = 50,000 \text{ DN}_2$, we find that a full-well pixel is subject to about 1000 DN_2 worth of traps as it is transferred from the top to the bottom of the detector (see Fig 6). On average, then, the trap at each individual level of q affects only 0.02 DN_2 of charge. Since the readnoise is about 2.5 DN_2 , it does not make sense to track the charge traps at this resolution. We can instead afford to parametrize the traps more intelligently.

We modified our routine to step through the traps not by every DN_2 in pixel value, but rather by every block of marginal charge that amounts to one DN_2 of traps. As a result we end up with a total of about 1000 traps, one at 1 DN_2 , one at 2 DN_2 , one at 4 DN_2 , then at 5, 6, 8 DN_2 , 10, 11, 13, 14, 15, 17 DN_2 , etc. The trap density is higher at lower charge levels, so at higher levels we skip for instance from 1000 to 1012. It is much quicker to keep track of only 1000 traps than 50,000. The difference in the model output is negligible, but the difference in execution time is enormous. We found that after this small change to the code, it ran about 6 times faster, doing 5 iterations on an entire 4096×4096 WFC image in about 10 minutes — a considerable improvement.

5.3. CTE in the Serial Direction

The possibility of imperfect CTE along the serial register (in the x direction) has been looked for in ACS images, but it has been found to be so low as to be unquantifiable (Riess & Mack ISR-2004-06). A cursory look at the dark stacks that we generated in § 2.2 shows

a curious x -hook in the direction away from the readout amplifier for the brighter warm pixels. Figure 23 shows a close-up of the region about $i = 2072$, which is the boundary where the serial readout direction changes from right-to-left to left-to-right in the full 4144×4136 images (See Figure 2). Below, we apply the same methodology to examine X-CTE that we used above for Y-CTE.

We return to the dark stack image from §2.2. For each of the significant warm pixels (i.e., those with peak-map hits of 125 or greater), we recorded the array of pixels from 5 pixels to its left to 5 pixels to its right. The schematic in Figure 4 shows which pixels were used to measure the serial trails. We constructed the empirical trails by subtracting the downstream pixels from the corresponding upstream pixels to remove the background. The excess in the first pixel in the trail can be seen by looking at $XU1 - XD1$, etc.

Figure 24 shows the first and second pixels in the trail as a function of distance from the serial register. The three panels from left to right show the trend for three different warm-pixel intensities. Clearly, the brighter the warm pixel, the brighter its trail. It is clear that there is a simple linear correlation between the first-pixel intensity and the distance from the serial register—a clear telltale sign of CTE loss. Surprisingly, the intercept in the relation is not at $i = 0$ but somewhere around $i = -500$, which is likely due to an effect caused by the new ASICs called the “bias-shift” (see Golimowski et al. 2010 for a discussion.)

Figure 25 shows the profile of the X-CTE trails for six different bins of WP intensity. The first-pixel intensity goes from about 1% of the WP at the faint end, to about 0.4 % at the bright end. There is very little noticeable flux in the second and subsequent pixels, so the serial CTE trails are quite different in nature from the parallel trails. This makes sense, as the dwell-time for charge packets in the parallel shifts is more than 2000 times longer than for the serial shifts ($22 \mu s$). This result is also consistent with expectation from theory

and laboratory experiments, which show that the trap-capture time is short compared to the parallel-shift time, but long compared to the serial-shift time (Cawley et al 2001).

The serial trails we see in the WFC are so short that they will have essentially no impact on aperture photometry, even for the smallest conceivable apertures. It is therefore not surprising that it has not yet been observed in photometry (Riess & Mack ISR 2004-06).

Since it is important to verify that the short trails we see do in fact contain all of the flux, meaning that no photometric correction will be necessary, we examined the photometric residuals against x as we had measured them against y . We found no significant signature of serial CTE losses in the photometry. Clearly almost all of the serial-CTE trails are extremely local.

The local nature of these trails does not, however, mean that it is not important to correct them. Since the trails have different amplitudes as a function of pixel value, this will have a disparate impact on stellar astrometry: the faint stars will appear to be shifted by ~ 0.01 pixel away from the readout amplifier, while the brighter stars will appear to be shifted by only ~ 0.004 pixel. (We infer this by simply reading off the first-pixel fractions from Figure 25). For a given star, this may be within most margins of error, but projects that involve analyzing the motions of many stars to determine the average motion for one population relative to another can, in principle, get precisions below 0.001 pixel. Such studies will be very susceptible to X-CTE biases. The prescription we suggest for parallel CTE in the preceding analysis should also be amenable to CTE correction in the serial direction. Indeed, since the trails are much more local, it should be much simpler to converge on the model parameters.

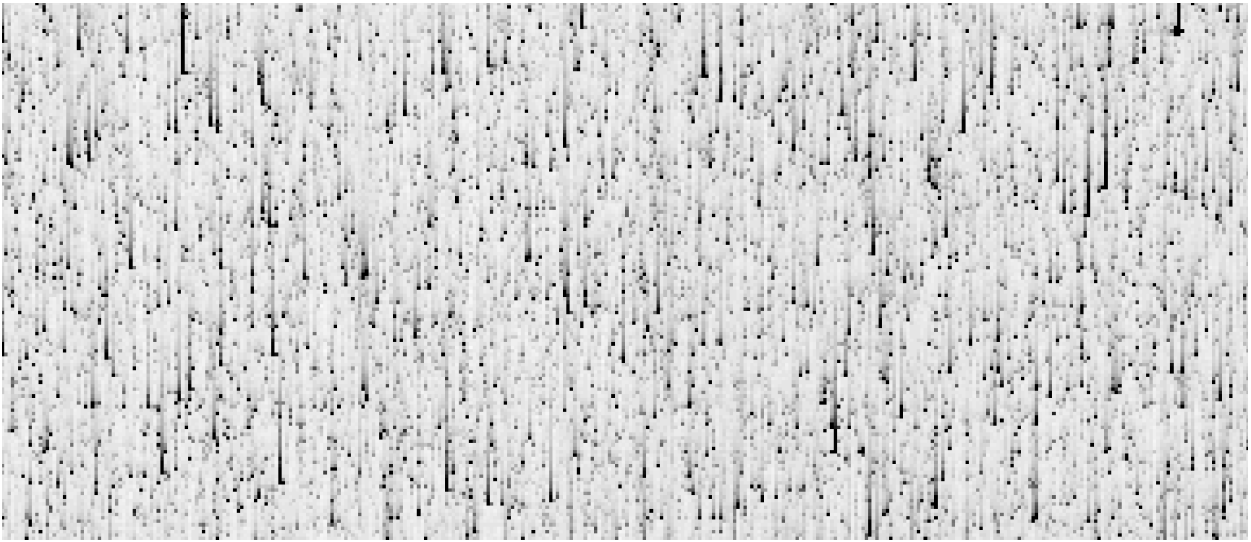


Fig. 23.— The region of the dark stack centered on pixel (1860,2172). The bright WPs show a clear x -hook towards the center of the image and away from the amplifier. Pixels are shifted leftward in the left half of the image, and rightward in the right half of the image.

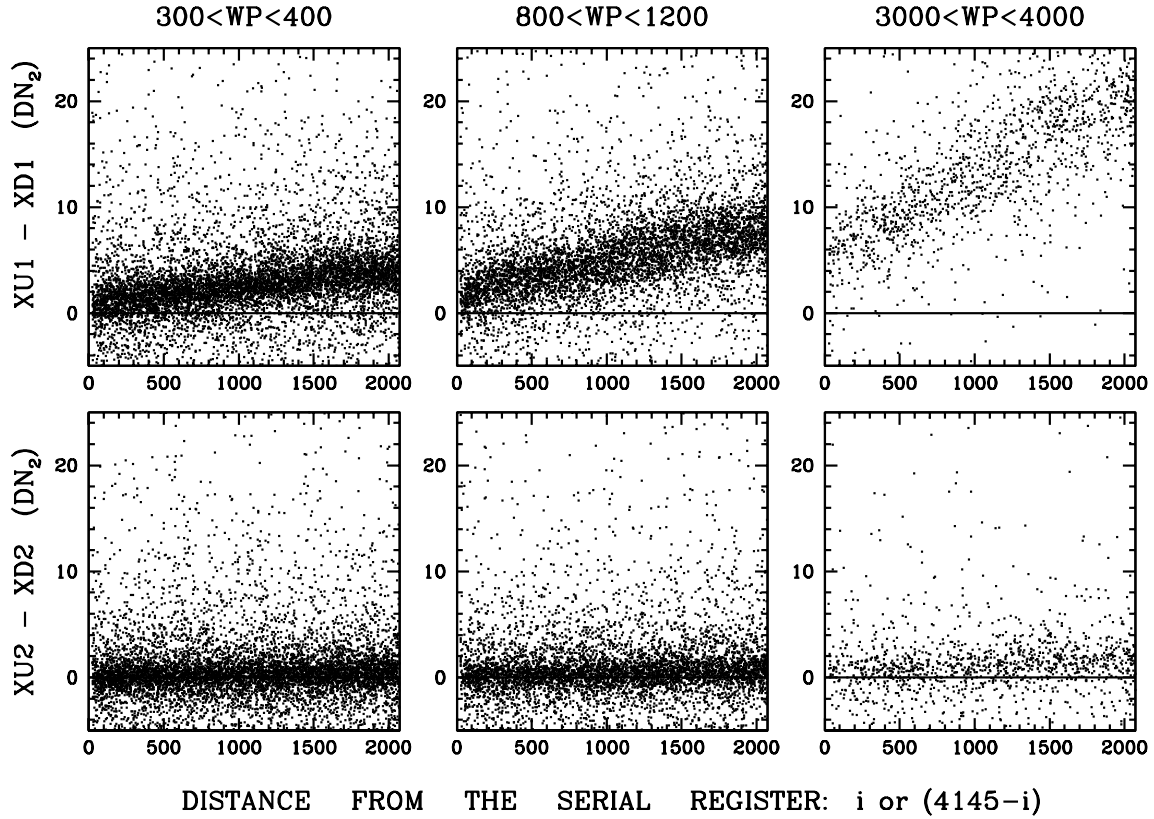


Fig. 24.— (Top) For three different intensities of warm pixel, we show the number of DN_2 in the first pixel in the serial trail as a function of the number serial shifts to the readout amplifier. (Bottom) We show the same for the second pixel in the serial trail.

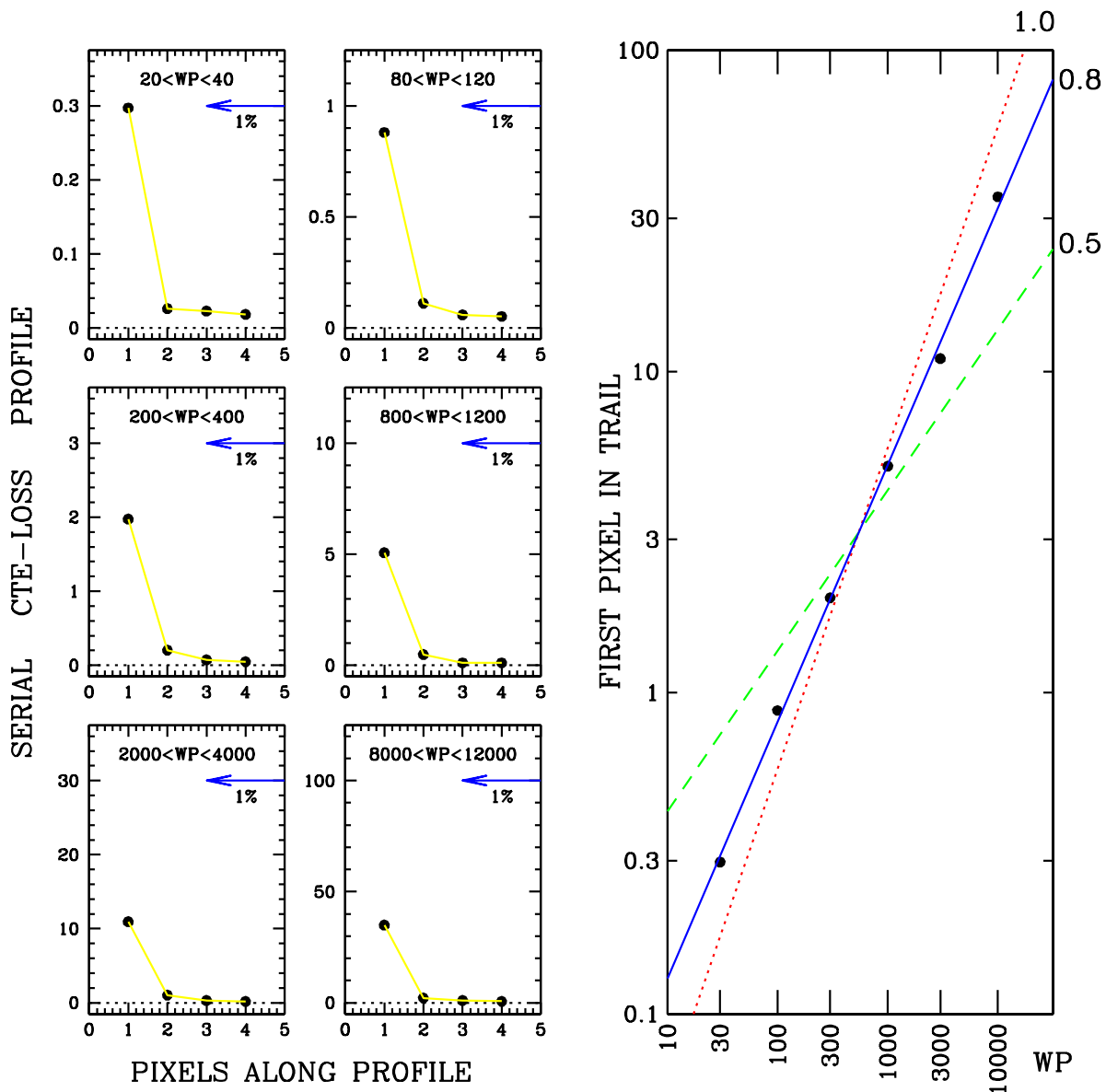


Fig. 25.— The panels on the left show the first four pixels in the serial-CTE trails for six different warm-pixel intensity bins, labeled at the top of each panel. The arrow in each plot shows the 1% level relative to the WP intensity: the first pixel intensity goes from 1% at $\sim 30 \text{ DN}_2$ to less than 0.4 % at $\sim 10,000 \text{ DN}_2$. The right panel shows the intensity of the first pixel in the trail as a function of the warm pixel intensity. The slopes for the power laws drawn in are indicated on the upper right.

6. SUMMARY AND NEXT STEPS

It has not been the goal of this document to create the definitive black-box prescription for fixing CTE losses in ACS/WFC images. Rather, our aim has been simply to demonstrate a proof-of-concept. There are clearly many improvements that can be made, and we will anticipate some of them below.

6.1. Accomplishments of the model

We have shown that it is indeed possible to simulate the readout mechanism for a CCD detector by means of a simple empirical model. This simulation can then be used to compute for us the probable initial distribution of charge amongst the pixels for a given read-out image.

Our model addresses the two long-standing concerns about imperfect CTE: the removal of the trails downstream of bright sources and the restoration of flux to the pixels where it originated. The algorithm was tailored to remove the trails from warm pixels in dark exposures, but we have shown (§3.11) that it works equally well for backgrounds up to $\sim 35 e^-$, with no reason to think it would not work for higher backgrounds, where the CTE impact is lower. We have shown that when it removes the trails from stars (§4.1), it puts all the flux back into the right place so that the star is measured to have the right brightness and the right position, as well (§4.3 and §4.4). We even showed in §4.6 that restored stars have the right shape, as well.

One of the shortcomings of any deconvolution procedure is its sensitivity to noise. Read-out noise, in particular, arises after the charge-transfer errors have been imprinted on the pixels, so we want to be certain that our algorithm does not over-correct artifacts that are unrelated to CTE. Our simulations show that by applying our algorithm blindly, we

could increase the effect of read-out noise by almost 40%. We have devised a conservative mechanism whereby our procedure only operates on the structure in the image that is clearly consistent with not being readnoise. This procedure reduces the impact of readnoise amplification to less than 3%.

We have used the same procedure to examine CTE in the serial direction. Traps in the serial register are extremely short-lived. They affect at most 1% of the charge in a pixel and release the charge within one transfer. This will have a negligible effect on photometry, but will have a small but non-negligible effect on astrometry. It should be possible to correct for serial CTE losses in a similar manner to our parallel correction.

The model we have developed clearly has the flexibility to address the observable aspects of CTE, even though it is silent on the unobservable aspects, such as what happens at each specific stage of the three-phase pixel shift or exactly how many trap species with different release profiles there are. These unobservable details may have a lot to do with what actually leads to charge-transfer errors, but it is possible to address CTE issues without answering these questions directly. Perhaps the clarity of our model will help experts develop a more detailed theoretical understanding of the phenomenon, and this improved understanding will surely yield even better corrections.

The model has been parametrized to allow a straightforward hand-fitting to the particulars of any detector. This approach can and should be attempted on other HST instruments, such as the HRC, WFPC2, STIS, and perhaps even WFC3 once the CTE errors rise to a measurable level. There may also be other non-HST detectors for which this model might prove useful.

6.2. Future Plans

There remain many avenues yet to pursue. This paper has focused exclusively on post-SM4 observations, where the CTE losses are as large as they have ever been. It should be straightforward to extend this analysis to earlier epochs by simply scaling down the amplitude of our parameters. While the WFC’s electronics board was replaced, the readout timing is unchanged and we expect our CTE model to work with essentially the same parameters for pre-SM4 data. This will need to be demonstrated, however. It will also be important to examine WP trails to study how CTE may or may not be impacted by anneals and temperature changes. Laboratory experiments (Janesick 2001) have shown that the trap-release time is faster for higher temperatures, so perhaps the trails will be even easier to model before the temperature was changed from -77°C to -81°C in 2006.

Our model has treated each pixel as being identical to all the others in terms of having the same distribution of electron-capturing traps. Since the traps are presumed to result from individual radiation-damage events, in actuality the pixel array will have a finite number of traps, each of which affects a specific level of charge packet. On average, every other pixel will be impacted by a trap at one depth or another, such that we might expect $1000 \pm \sqrt{1000}$ traps in each 2048-pixel column. A variation of 3% would not seem important. However, if the trap-creating events generate multiple traps at once, as is expected for energetic neutron or ion impacts, then we might expect more variation than this from column to column, which might make our corrections less effective. We attempted to look into this by examining the corrections of CR trails, but did not see a significant and consistent column-by-column effect. Perhaps the best way to evaluate this would be to examine the efficacy of the photometric correction for stars of known brightness as a function of column number. With the many sets of short+deep exposures in the archive of fields with good numbers of stars, it should be possible to rack up hundreds of star

observations in each column.

The model we constructed is based on a representation of the density of traps that affect electron packets with various amounts of charge. It was difficult to constrain the trap density at the charge extremes. There were very few warm pixels with more than 10,000 DN_2 in the ~ 1000 s integration. As such, we had relatively few constraints on the density of traps that affect the electron packets at the bright end. This node in the Φ_Q array might be better constrained by studying stars in short+deep combinations of images.

At the low-intensity extreme, it was hard to identify warm pixels with fewer than 10 DN_2 at the top of the register, since this is so close to the readnoise level and since these low WPs are so smeared out by CTE losses. These issues could be further investigated using warm pixels closer to the register, where the expected number of traps encountered per electron might be much less than one. It would be good to understand the low end of the density profile, even though there may still be nothing that can be done to restore the image. It would also be good to take some shorter dark exposures, so that we can use our knowledge of the true intensity of the WPs from the deep darks to study how CTE impacts the smaller electron packets. Also, with shorter darks, the crowding of WPs at the low- DN_2 level would be significantly lessened. The ACS team is looking into taking darks with a variety of exposure times to explore these issues.

The model itself is designed to treat CTE losses as a perturbation. We adopted the simplification that it is possible to treat the transfer of flux from a pixel 2000 pixels from the register as having simply $2000 \times$ CTE losses of a single transfer. Essentially, we are assuming that $(CTE)^N \approx 1 - N \times (1 - CTE)$. This assumption should be revisited. While it would be prohibitive to treat individually each and every one of the 2048×1024 pixel-to-pixel

shifts that take place in each column⁷, it should be possible to find a happy medium where we can still safely treat imperfect CTE as a perturbation within each modeled transfer. One solution to this would be to run the algorithm three times in succession, using only one-third the current-model scaling. This would ensure that CTE losses are indeed treated as a small perturbation within each iteration. We have begun experimenting with this, but are awaiting shorter dark exposures to provide more useful tests. One early result worth mentioning is that in this iterative scheme, where losses are kept at the perturbation level, the parameters of our model will naturally change somewhat, and we find that the trail profiles for the low-intensity WPs become more like those for the high-intensity trails, such that all WPs have the same trail profile. This result makes sense in light of the explanation in (Hardy et al. 1998) about how the traps that impact low- and high-intensity packets differ only in terms of their location within the lattice relative to the pixel boundaries. As such, their release profiles should sensibly be the same. This will be pursued in future work (Paper II), once the shorter darks are in hand.

Finally, the possibility of correcting for imperfect CTE at the source could have profound implications for how best to operate the ACS pipeline. Should a CTE algorithm such as this one be executed on images before they are pipeline-processed, or is this best done after-market, and only by those who really need it? Might the optimal approach depend on the science goals? To highlight these complications, we note that our entire analysis has been premised on the fact that the dark images that we downloaded do *not* really reflect just the raw dark current in each pixel. Rather, the true dark-current image has clearly been smeared out by the CTE-afflicted readout process. Science images will suffer differing amounts of warm-pixel smearing depending on their background and exposure time; as such there is no single dark image that can be scaled up to estimate

⁷ The typical pixel is shifted down 1024 rows, and there are 2048 pixels in each column.

the impact of dark current and warm pixels on each pixel for any integration. Addressing this properly will require much thought, but there probably is not a single “right” way to deal with this. Bristow (2004) fleshes out some of the issues involved in considering such a CTE-pre-processor for STIS.

An additional consideration that arises when dealing with this correction as a part of the pipeline is what should be done with the error image that is provided along with the calibrated science image. The CTE correction cannot be done perfectly, and the corrected image may have some systematic errors related to the imperfection of the algorithm and some random errors related to the fact that any deconvolution-type algorithm tends to amplify readnoise. It will be important to run astrometric and photometric tests on standard fields to come up with an effective way to represent these errors.

We have provided the details of our algorithm in this report, but have not yet made public the actual code. This is because the algorithm is currently being evaluated by the Institute to determine whether and how best to implement it in the various data products. Some version of it should be available shortly.

We acknowledge Linda Smith, ACS Team Lead, and David Golimowski for helpful discussions and encouragement. We are also grateful for many invaluable discussions about CTE with Paul Goudfrooj, Andy Fruchter, Jennifer Mack, Adam Riess, Stefano Casertano, Marco Chiaberge, and many others. We are grateful to the anonymous referee for pointing us to several articles that discuss results of laboratory testing. Such articles often do not show up on astronomical search engines, and were glad to be made aware of them. Finally, J.A. acknowledges Oleg Gnedin (PI of GO-10824 and GO-11589) for his patience in waiting for the hyper-velocity-star proper-motion measurements that this correction should make possible.

REFERENCES

- Anderson, J. & King, I. R. 2000 PASP 112 1360
- Anderson, J. & King, I. R. 2006, ACS/ISR 2006-01, *PSFs, Photometry, and Astrometry for the ACS/WFC*
- Anderson, J. 2007, ACS/ISR 2007-08, *Variation of the Distortion Solution of the WFC*
- Anderson, J., Piotto, G., King, I. R., Bedin, L. R., Guhathakurta, P. 2009, ApJ, 697L, 58, *Mixed Populations in Globular Clusters. Et Tu, 47 Tuc?*
- Biretta, J. & Mutchler, M. 1997 ISR WFPC2 97-05 *Charge Trapping and CTE Residual Images in the WFPC2 CCDs*
- Biretta, J. & Kozhurina-Platais, V. 2005 WFPC2 ISR/05-01 *Hot Pixels as a Probe of WFPC2 CTE Effects*
- Bristow, P. & Alexov, A. 2002, CE-STIC-2002-001, *Modelling Charge-Coupled Device Readout: Simulation Overview and Early Results*
- Bristow, P. 2003a CE-STIS-2003-001, *Application of Model-Derived Charge Transfer Inefficiency Corrections to STIS Photometric CCD Data*
- Bristow, P. 2003b CE-STIS-2003-002, *Application of Model-Derived Charge Transfer Inefficiency Corrections to STIS Spectroscopic Data*
- Bristow, P. 2004 CE-STIS 2004-002, *The Impact of the CTI-correction Pre-Processor upon Standard STIS CCD Pipeline Dark and Bias Reference Files*
- Cawley, L., Goudfrooij, P., Whitmore, B., Stiavelli, M., et al. 2001- WFC3 ISR 2001-05, *HST CCD Performance in the Second Decade: Charge Transfer Efficiency*
- Chiaberge, M., Lim, P.-L., Kozhurina-Platais, V., Sirianni, M. & Mack, J. 2009, ACS/ISR 2009-01, *Updated CTE Photometric Correction for WFC and HRC*

Dolphin, A. E. 2000, PASP, 112, 1397

Dolphin, A. E. 2009, PASP, 121, 655

Golimowski, D. et al. 2010, ISR in prep.

Goudfrooij, P., Bohlin, R. C., Maíz-Appellaníz, J. & Kimble, R. A. 2006, PASP, 848, 1453

Grogin, N. et al. 2010, ISR in prep.

Hardy, T., Murowinski, R., & Deen, M. J. 1998 IEEE Transaction on Nuclear Science Vol 45
N2 1998 p154

Janesick, J., Soli, G., Elliott, T., & Collins, S. 1991 SPIE Vol 1447 Charge-Coupled Devices and
Solid State Optical Sensors II

Janesick, J. R. Scientific Charge-Coupled Devices 2001 SPIE Press monograph, Bellington,
Washington.

Kozhurina-Platais, V., Goudfrooij, P., & Puzia, T. H. 2007 ACS/ISR 2007.04, *ACS/WFC:
Differential CTE corrections for Photometry and Astrometry from non-drizzled images*

Massey, R., Stoughton, C., Leauthaud, A., Rhodes, J., Koekemoer, A., Ellis, R., Shaghoulain,
E. 2010, MNRAS, 401, 371

Maybhate, A. et al. 2010 ACS Instrument Handbook, Version 9.0 (Baltimore: STScI)

McLaughlin, D. E., Anderson, J., Meylan, G., Gebhardt, K., Pryor, C, Minniti, D., & Phinney,
S. 2006, ApJS, 166, 249 *Hubble Space Telescope Proper Motions and Stellar Dynamics in the
Core of the Globular Cluster 47 Tucanae*

Mutchler, M. & Sirianni, M. 2005, ACS/ISR 2005-03, *Internal Monitoring of ACS Charge
Transfer Efficiency*

Philbrick, R. H., Ball Aerospace & Technologies Corp. 2001, *Modelling the Impact of
Pre-flushing on CTE in Proton Irradiated CCD based Detectors*

Riess, A. 2000, WFPC2/ISR 2000-04, *How CTE Affects Extended Sources*

Riess, A. & Mack, J. 2004, ACS/ISR 2004-06, *Time Dependence of ACS WFC CTE Corrections for Photometry and Future Predictions*

Sirianni et al 2007, IEEE Radiation Effects Data Workshop *Radiation Damage in Hubble Space Telescope Detectors*

Waczynski et al 2001 IEEE Transaction on Nuclear Science Vol 48 N 6 2001 pag 1807